



Spectral Classification and Ionized Gas Outflows in $z \sim 2$ *WISE*-selected Hot Dust-obscured Galaxies

Hyunsung D. Jun^{1,2}, Roberto J. Assef³, Franz E. Bauer^{4,5,6}, Andrew Blain⁷, Tanio Díaz-Santos⁸,
 Peter R. M. Eisenhardt², Daniel Stern², Chao-Wei Tsai⁹, Edward, L. Wright¹⁰, and Jingwen Wu⁹

¹ School of Physics, Korea Institute for Advanced Study, 85 Hoegiro, Dongdaemun-gu, Seoul 02455, Republic of Korea; hsjun@kias.re.kr

² Jet Propulsion Laboratory, California Institute of Technology, 4800 Oak Grove Drive, Pasadena, CA 91109, USA

³ Núcleo de Astronomía de la Facultad de Ingeniería y Ciencias, Universidad Diego Portales, Av. Ejército Libertador 441, Santiago, Chile

⁴ Instituto de Astrofísica and Centro de Astroingeniería, Facultad de Física, Pontificia Universidad Católica de Chile, Casilla 306, Santiago 22, Chile

⁵ Millennium Institute of Astrophysics (MAS), Nuncio Monseñor Sotero Sanz 100, Providencia, Santiago, Chile

⁶ Space Science Institute, 4750 Walnut Street, Suite 205, Boulder, CO 80301, USA

⁷ Department of Physics and Astronomy, University of Leicester, LE1 7RH Leicester, UK

⁸ Núcleo de Astronomía de la Facultad de Ingeniería, Universidad Diego Portales, Av. Ejército Libertador 441, Santiago, Chile

⁹ National Astronomical Observatories, Chinese Academy of Sciences, 20A Datun Road, Chaoyang District, Beijing 100012, People's Republic of China

¹⁰ Department of Physics and Astronomy, University of California, Los Angeles, CA 90095, USA

Received 2019 August 21; revised 2019 November 18; accepted 2019 December 2; published 2020 January 15

Abstract

We present Very Large Telescope/XSHOOTER rest-frame UV–optical spectra of 10 hot dust-obscured galaxies (Hot DOGs) at $z \sim 2$ to investigate active galactic nucleus (AGN) diagnostics and assess the presence and effect of ionized gas outflows. Most Hot DOGs in this sample are narrow-line-dominated AGNs (type 1.8 or higher) and have higher Balmer decrements than typical type 2 quasars. Almost all (8/9) sources show evidence for ionized gas outflows in the form of broad and blueshifted [O III] profiles, and some sources have such profiles in H α (5/7) or [O II] (3/6). Combined with the literature, these results support additional sources of obscuration beyond the simple torus invoked by AGN unification models. Outflow rates derived from the broad [O III] line ($\gtrsim 10^3 M_\odot \text{ yr}^{-1}$) are greater than the black hole accretion and star formation rates, with feedback efficiencies ($\sim 0.1\%–1\%$) consistent with negative feedback to the host galaxy's star formation in merger-driven quasar activity scenarios. We find that the broad emission lines in luminous, obscured quasars are often better explained by outflows within the narrow-line region and caution that black hole mass estimates for such sources in the literature may have substantial uncertainty. Regardless, we find lower bounds on the Eddington ratio for Hot DOGs near unity.

Unified Astronomy Thesaurus concepts: Active galaxies (17)

1. Introduction

According to the triggering and evolution scenario for active galactic nuclei (AGNs) from gas-rich galaxy mergers (e.g., Hopkins et al. 2008; Hickox et al. 2009), the most vigorous accretion in AGNs occurs in between the dusty star-forming phase of the merger and the unobscured AGN phase. Gas inflowing toward the merging center is thought to trigger starbursts in a dusty environment, but then the onset of AGN activity introduces negative feedback by heating and pushing out the surrounding gas and dust, disrupting star formation (e.g., Silk & Rees 1998; Di Matteo et al. 2005; Croton et al. 2006; Fabian 2012). If there is effective radiative or kinetic energy transferred into the interstellar medium (ISM), the AGN host will become more transparent until the system becomes quiescent in both AGN and star formation activities.

The interaction between the accreting black hole (BH) and its environment in this scenario results in distinctive phases in BH–galaxy coevolution and corresponding types of observed galaxies related to each phase. Space-based infrared (IR) missions such as the *Infrared Astronomical Satellite* (Neugebauer et al. 1984), *Spitzer* (Werner et al. 2004), *Akari* (Murakami et al. 2007), and the *Wide-field Infrared Survey Explorer* (*WISE*; Wright et al. 2010) have discovered IR-luminous galaxies over a wide range of luminosity and reddening, sharing observed properties consistent with model predictions. Among the ultraluminous IR galaxies (ULIRGs, $L_{\text{IR}} > 10^{12} L_\odot$; Sanders et al. 1988), dust-obscured galaxies

(DOGs, $F_{\nu, 24\mu\text{m}} > 0.3 \text{ mJy}$, $F_{\nu, 24\mu\text{m}}/F_{\nu, R\text{-band}} \geq 1000$; Dey et al. 2008) show large amounts of IR emission from dust heated by a mixed contribution of AGN and star formation activities at $z \sim 2$, as opposed to the starburst dominance found in submillimeter galaxies (SMGs; Blain et al. 2002; Chapman et al. 2005) at similar luminosity and redshift. Within the merger-triggered AGN evolution scenario in ULIRGs, SMGs are thought to represent an early phase of gas-rich merger-driven starburst, followed by AGN activity taking place in DOGs and clearing out of the AGN surroundings (e.g., Dey et al. 2008; Narayanan et al. 2010). This so-called blowout phase should be observed as AGN outflows in DOGs, as they become transparent and evolve into optically luminous quasars.

With the advent of the *WISE* space mission, a similar selection to DOGs was made possible using just the mid-IR flux and color. Objects with W3 (12 μm) or W4 (22 μm) fluxes an order of magnitude brighter than DOGs, red mid-IR colors, and a faint W1 (3.4 μm) flux limit were discovered and named W1W2 dropouts, or Hot DOGs (Eisenhardt et al. 2012; Wu et al. 2012). Hot DOGs show comparably red $F_{\nu, 24\mu\text{m}}/F_{\nu, R\text{-band}}$ ratios to DOGs (e.g., Wu et al. 2012) but higher IR luminosities, pushing them into the HyLIRG ($L_{\text{IR}} > 10^{13} L_\odot$; Sanders & Mirabel 1996) or even ELIRG ($L_{\text{IR}} > 10^{14} L_\odot$; Tsai et al. 2015) regimes.

The spectral energy distributions (SEDs) of Hot DOGs are peaked in the mid-IR from dust-heated emission, which, together with the extreme IR luminosity, suggests the presence and dominance of obscured AGN activity over star formation

Table 1
Summary of Targets

Name	Coordinates (J2000)	z	Flag	L_{5100} (10^{46} erg s $^{-1}$)	$E(B-V)$ (mag)	W1 (mag)	t_{exp} (minutes)	Instrument (minutes)	Wavelength
W0114-0812	J011420.48-081243.7	2.1037 ± 0.0002	A	6.46	4.0	17.4	50	1	0.3–2.5 μm
W0126-0529	J012611.96-052909.6	0.8301 ± 0.0001	A	0.71	31.6	17.6	50	1	0.3–2.5 μm
W0147-0923	J014747.58-092350.8	2.2535 ± 0.0006	A	19.6	20.0	>18.6	100	1	0.3–2.5 μm
W0226+0514	J022646.87+051422.6	2.3613 ± 0.0005	A	9.71	10.6	17.7	100	1	0.3–2.5 μm
W1103-1826	J110330.08-182606.2	2.5069 ± 0.0006	A	7.34	5.5	17.7	100	1	0.3–2.5 μm
W1136+4236	J113634.29+423602.8	2.4077 ± 0.0002	A	3.47	2.8	18.2	30, 18	2	H, K
W1719+0446	J171946.63+044635.2	2.5498 ± 0.0012	A	11.3	3.1	17.6	50	1	0.3–2.5 μm
W2016-0041	J201650.30-004109.0	2.6121 ± 0.0005	B	7.01	3.2	17.9	50	1	0.3–2.5 μm
W2026+0716	J202615.22+071624.2	2.5695 ± 0.0007	A	6.09	3.6	17.6	50	1	0.3–2.5 μm
W2042-3245	J204249.28-324517.9	2.9583 ± 0.0058	B	21.6	7.4	>18.5	50	1	0.3–2.5 μm
W2136-1631	J213655.73-163137.8	1.6587 ± 0.0000	A	2.59	5.5	17.8	50	1	0.3–2.5 μm
W2216+0723	J221619.09+072353.3	1.6861 ± 0.0004	A	3.31	7.9	17.3	60	3	JH

Note. z : systemic redshift (Section 4.1); flag: quality of the redshift; L_{5100} : rest-frame 5100 Å AGN luminosity; $E(B-V)$: extinction from Assef et al. (2015); W1: ALLWISE 3.4 μm Vega magnitude (Wright et al. 2010); t_{exp} : exposure time; instrument: VLT/XSHOOTER (1), Keck/MOSFIRE (2), Gemini/FLAMINGOS-2 (3).

(e.g., Wu et al. 2012; Stern et al. 2014; Assef et al. 2015; Tsai et al. 2015). Near-IR through submillimeter imaging observations have also identified their \sim arcminute-scale environment to be overdense (e.g., Jones et al. 2014; Assef et al. 2015), consistent with a luminous, obscured AGN triggered by mergers of galaxies (e.g., Fan et al. 2016; Ricci et al. 2017b; Díaz-Santos et al. 2018; but see also Farrah et al. 2017). Furthermore, these obscured AGNs are nearly as numerous as unobscured AGNs at comparably high luminosity (e.g., Assef et al. 2015; Banerji et al. 2015; Lacy et al. 2015). Hot DOGs are therefore good test beds to search for strong feedback in action in the most luminous, obscured, and potentially merger-driven AGNs.

Previous studies have reported ionized gas outflows traced by the broad and blueshifted motion of the [O III] emission line, not only in $z \lesssim 1$ type 2 AGNs (e.g., Crenshaw & Kraemer 2000; Greene & Ho 2005a; Villar-Martín et al. 2011 hereafter V11; Liu et al. 2013; Mullaney et al. 2013; Bae & Woo 2014; Zakamska & Greene 2014; Woo et al. 2016; DiPompeo et al. 2018) but also in highly obscured and luminous $z \sim 1$ –3 AGNs, where feeding and feedback are expected and observed to be stronger (e.g., Greene et al. 2014; Brusa et al. 2015 hereafter B15; Cresci et al. 2015; Perna et al. 2015; Zakamska et al. 2016 hereafter Z16; Leung et al. 2017; Toba et al. 2017; Perrotta et al. 2019; Temple et al. 2019).

The diversity of reddening in AGNs, however, is often explained by a mixture of evolutionary and orientation effects (e.g., Jun & Im 2013; Shen & Ho 2014; Glikman et al. 2018). Conventionally, the type 1/2 classification for AGN spectra (e.g., Osterbrock 1981) was interpreted to be an orientation effect of the central obscuring structure to our line of sight (e.g., Antonucci 1993; Urry & Padovani 1995), although there have been substantial modifications in response to subsequent observations (e.g., Hönig & Beckert 2007; Nenkova et al. 2008). According to the simplest orientation model, outflows in obscured type 2 AGNs will appear weaker due to a smaller line-of-sight motion of the outflowing material viewed edge-on.

To better assess the importance of obscured AGN feeding and feedback, as well as provide AGN diagnostics to differentiate between the simplest form of obscuration models and help constrain the spatial extent of dust, we obtained rest-frame UV–optical spectra for 10 Hot DOGs with the Very Large Telescope (VLT) XSHOOTER. In this paper, we

describe our sample and data (Section 2), analyze the spectra (Section 3), and present the redshifts, line ratios, and derived accretion and outflow quantities (Section 4). A flat, Λ CDM cosmology with $H_0 = 70 \text{ km s}^{-1} \text{ Mpc}^{-1}$, $\Omega_m = 0.3$, and $\Omega_\Lambda = 0.7$ (e.g., Im et al. 1997) is used throughout.

2. Data

2.1. Sample Description and Observations

Our targets, listed in Table 1, were selected to probe the rest-frame UV-to-optical spectral properties of $z \sim 2$ Hot DOGs, complementing our observation programs using the Keck and Gemini telescopes to investigate BH accretion using the $H\alpha$ line (Wu et al. 2018). The XSHOOTER sample consists of 10 galaxies, some with existing redshifts at the time of writing the observation proposal (6/10). The remainder (4/10) were targeted with the added goal of securing a redshift. The color selection for heavily obscured, W1W2-dropout sources naturally prefers the rise in the near-to-mid-IR SED by dust-heated emission from the AGN located in the W3 band or longer wavelengths, corresponding to $z \gtrsim 2$ (see also Ricci et al. 2017a for biases against $z \lesssim 1$).

To illustrate where our targets lie in obscuration and luminosity with respect to other populations of luminous, obscured AGNs, Figure 1 plots the AGN extinction derived from photometric SED fitting against the AGN luminosity.¹¹ The XSHOOTER target samples the $E(B-V)$ – L_{bol} space, similar to the optical spectroscopic “full sample W1W2 dropouts” in Assef et al. (2015), spanning the highest luminosity and extinction values. Hot DOGs have $E(B-V)$ values of a few to tens of mag and are up to an order of magnitude more obscured than nearly as luminous, heavily reddened type 1 quasars (Banerji et al. 2012, 2013, 2015; Temple et al. 2019), red type 1 quasars (Glikman et al. 2012), or extremely red type 1/2 quasars (Ross et al. 2015) with $E(B-V) \lesssim 1.5$ mag. Estimating $E(B-V)$ values for obscured AGNs can be quite sensitive to the method. Our values are derived from the photometric SED fitting as described in

¹¹ Throughout, a bolometric correction of 9.26 (Richards et al. 2006; Shen et al. 2011) is used to convert the extinction-corrected 5100 Å luminosity (L_{5100}).

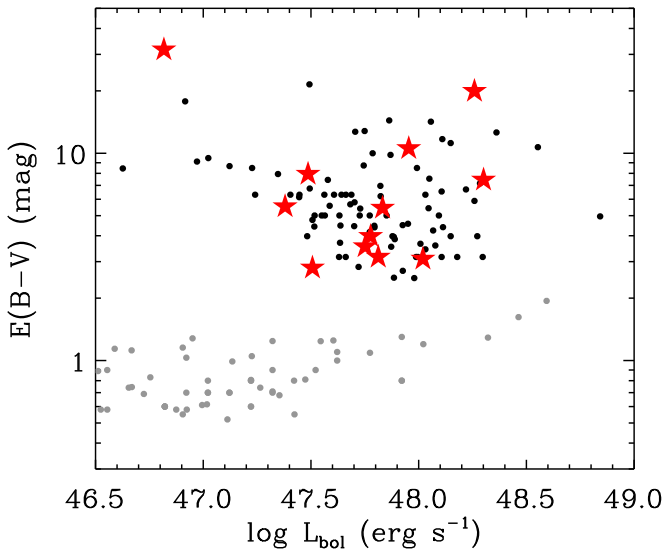


Figure 1. Broadband SED fit-based extinction-bolometric luminosity diagram for Hot DOGs (Assef et al. 2015; black dots). The XSHOOTER sample is shown by red stars. Red quasars and heavily reddened quasars (Banerji et al. 2012, 2013, 2015; Urrutia et al. 2012 hereafter U12; Kim & Im 2018; Temple et al. 2019; gray dots) are shown for comparison.

Assef et al. (2015). When compared to $E(B-V)$ values measured by comparing modeled-to-observed *WISE* W2 flux ratios, the latter $E(B-V)$ values are smaller by about a factor of 2 but do not change the main results of this work.

The XSHOOTER (Vernet et al. 2011) instrument on the VLT was used to collect simultaneous 0.3–2.5 μm spectra of the targets, cross-dispersed along its three arms (UVB, VIS, and NIR). Due to the wide spectral coverage, XSHOOTER is capable of extracting multiple emission lines across the observed spectrum and obtaining a secure redshift. Slit widths of 1", 1"2, and 1"2 were adopted for the UVB, VIS, and NIR arms, yielding spectral resolutions of $R = 4290$, 3360, and 3900, respectively. The data were taken under program 095.B-0507 in 2015 April through September. Each target was observed for either five or 10 frames (449 s in UVB, 600 s in VIS, 514 s in NIR per frame), depending on its H -band magnitude (Assef et al. 2015). We used an ABBA nodding mode. Calibration stars were observed for each target, as well as arcs for spatial and wavelength calibrations. Typical airmasses during the observations were 1–1.2, with seeing around 1" and precipitable water vapor of 2–3 mm. The observations are summarized in Table 1. In addition to the XSHOOTER spectra, we include previously published Keck/MOSFIRE H - and K -band spectra ($R \sim 3600$) for *WISE* J113634.29+423602.8 and Gemini/FLAMINGOS-2 JH -band ($R \sim 1000$) spectra for *WISE* J221609.09+072353.3 from Wu et al. (2018).

Supplementing the spectra, we compiled rest-frame optical-to-mid-IR photometry-based measurements of L_{bol} from Assef et al. (2015), estimated based on the best-fit AGN template after removing host contamination and correcting for obscuration. For unobscured AGNs, the monochromatic 5100 Å bolometric correction has been widely used to estimate bolometric luminosities from a limited number of photometric bands (e.g., Richards et al. 2006). In the case of extremely obscured AGNs such as Hot DOGs, one could either (i) make a reddening correction from the photometric SED and apply a

monochromatic bolometric correction (e.g., 5100 Å in Assef et al. 2015), (ii) directly integrate along the observed wavelengths without a bolometric correction (e.g., rest-frame UV to far-IR in Tsai et al. 2015), or (iii) make a compromised integration of the best-fit model (e.g., Z16). The first option provides a simple bolometric correction without requiring continuous coverage of the SED, while the second two options allow estimates based on the simple shape of the SED dominated by the mid-IR AGN torus emission: we adopt the Assef et al. (2015) formalism (option (i)) for a fair comparison to other studies.

2.2. Data Reduction

The ESO Science Archive Facility provides phase-3 data products reduced with the Reflex pipeline (Freudling et al. 2013). The reduction steps include bias, dark, and flat corrections; wavelength and spatial scale calibrations; flux calibration; combination of frames with cosmic-ray rejection; and trace and 1D extraction. In addition to these standard steps, we performed a telluric absorption correction using Molecfit (Kausch et al. 2015; Smette et al. 2015). Using the standard stars selected close to the target in altitude and azimuth and observed before or after the science target with the same instrument configuration, we obtained the telluric correction. Visual inspection of the pipeline-processed spectra showed some strongly outlying pixel values outside the telluric bands. We removed these using an absolute signal-to-noise ratio (S/N) threshold of 30–300 times the median S/N, depending on target, but with an uncertainty still less than five times the median noise. These cuts removed 0.15% of the data, on average, while keeping the emission line profiles unchanged.

Our data, with five or 10 frames, suffer from an insufficient number of frames to fill multiples of four, the number used for a single nodding sequence by the standard ABBA nodding mode reduction pipeline. We therefore use the phase-3 data, which only keep 4/5 or 8/10 frames due to the pipeline limitations. Assuming that object photon noise follows a Poisson distribution, this is an 11% hit on the S/N. When we used eight frames, or twice the nodding sequence, we averaged the flux and propagated the errors from each sequence. When compiling the reduced data coming from adjacent arms, overlapping data near the dichroics (0.560 and 1.024 μm) were trimmed to where both sides of the arms have comparable S/Ns by constraining $\lambda_{\text{UVB}} < 0.565 \mu\text{m}$, $0.555 \mu\text{m} < \lambda_{\text{VIS}} < 1.03 \mu\text{m}$, and $1.02 \mu\text{m} < \lambda_{\text{NIR}} < 2.40 \mu\text{m}$. Lastly, we applied Galactic extinction corrections assuming $R_V = 3.1$ and $E(B-V)$ values from the Schlafly & Finkbeiner (2011) extinction map.

In Figure 2, we plot the reduced, rest-frame 800–7000 Å spectra with available photometric fluxes and 2σ upper limits from Assef et al. (2015). Apart from the two spectra from Wu et al. (2018) missing the rest-UV wavelengths, the spectra cover major UV-optical emission lines. The average and 1σ scatter of the continuum S/N¹² are 0.9 ± 1.1 . This is not a critical issue, as we focus on the brighter lines, and we apply S/N cuts when analyzing the lines in the forthcoming sections. We binned the spectra matched to the spectral resolution of each arm for analysis.

¹² Throughout, we measure the continuum S/N per resolution element and the line S/N over wavelengths within $\pm\text{FWHM}$ from the line center, except [S II], where we use the flux and uncertainty of the combined doublet.

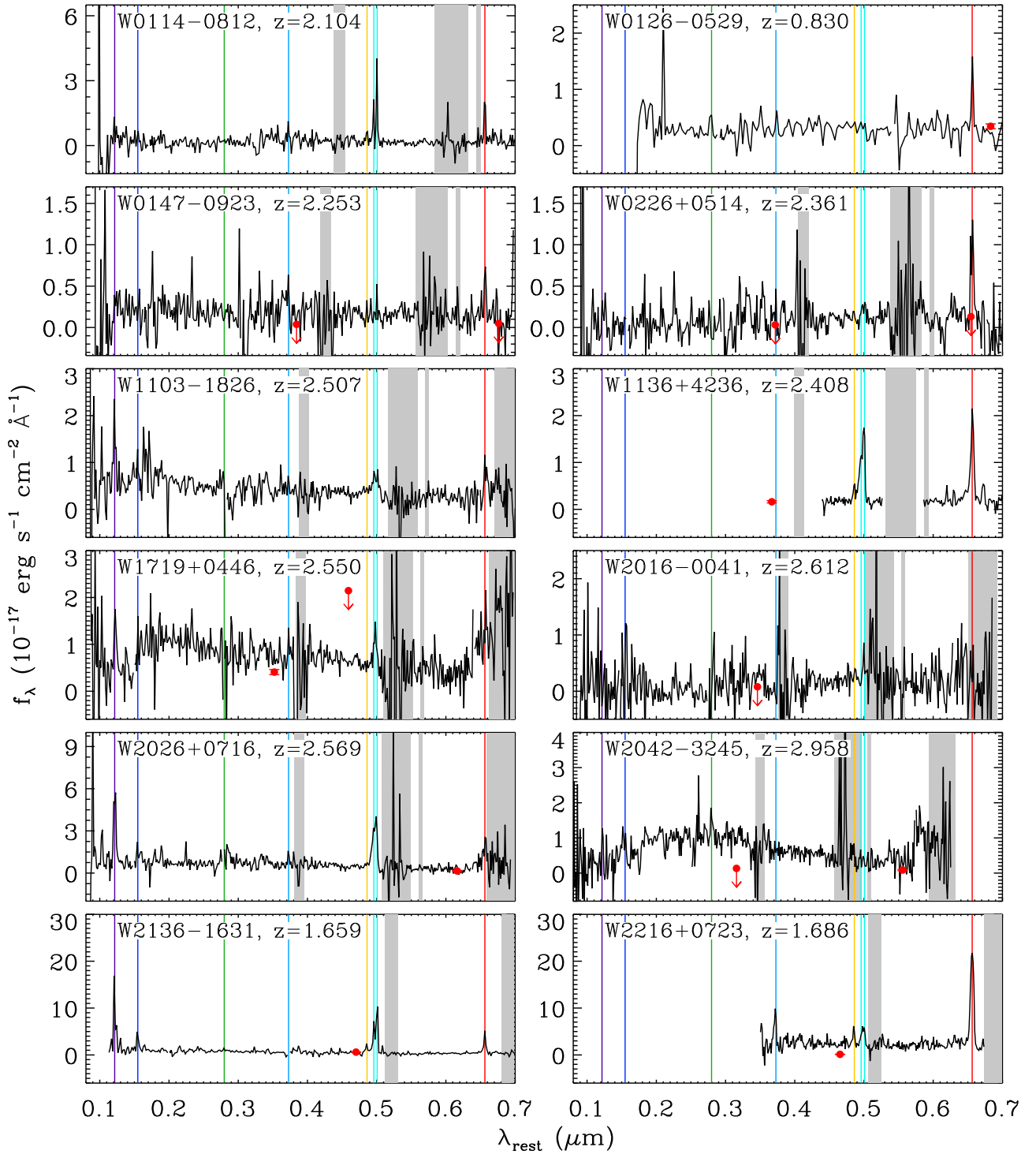


Figure 2. Reduced and extracted rest-frame spectra of the sample (black), binned down to $R = 100$, 100, and 800 for the UVB, VIS, and NIR arms for the sake of display. Photometric data points (red) are from Assef et al. (2015). Wavelengths with strong telluric absorption or sky background are shaded (gray), and noticeable lines ($\text{Ly}\alpha$, C IV, Mg II, [O II] $\lambda 3727$, H β , [O III] $\lambda 4959/5007$, H α) are marked with color-coded vertical lines in order of increasing wavelength. Discontinuities in the spectra are from different arm data.

3. Analysis

Taking advantage of the simultaneous wide spectral coverage of XSHOOTER, we fit the rest-frame 1150–2000, 2000–3500, and 3500–7000 Å regions, each containing multiple key emission lines (e.g., $\text{Ly}\alpha/\text{C IV}$, Mg II, and Balmer and [O III] lines, respectively). Regions of strong telluric correction (e.g., 1.36–1.41, 1.81–1.96, and 2–2.02 μm) or high sky

background (2.4 μm and longer) are masked from the fits. We split the fitting regions into three to account for the shapes of the (i) thermal UV bump from the accretion disk, (ii) Balmer continuum, (iii) broad absorption features, (iv) internal extinction, and (v) host galaxy contamination that can complicate either fitting a simple power-law continuum through the entire wavelength range or separately constraining

Table 2
Fitting Configuration

Line	Gaussians	Center	FWHM	Flux	Flux Ratio
Ly α λ 1215	N+B	1,2	9,10	17,18	...
N V λ 1240	N+B	1,2	9,10	19,20	...
C IV λ 1549	N+B	1,2	9,10	21,22	...
Si III] λ 1892	N+B	1,2	9,10	23,24	...
C III] λ 1908	N+B	1,2	9,10	25,26	...
Mg II λ 2798	N+B	3,4	11,12	27,28	...
[Ne V] λ 3426	N+B	3,4	11,12	29,30	...
[O II] λ 3727	N+B	5,6	13,14	31,32	...
H γ λ 4340	N+B	5,6	13,14	33,34	...
[O III] λ 4363	N	5	13	35	...
H β λ 4861	N+B	5,6	13,14	36,37	...
[O III] λ 4959/5007	N+B	7,8	15,16	38,39	2.98
[O I] λ 6300	N	5	13	40	...
[N II] λ 6548/6583	N	5	13	41	2.96
H α λ 6563	N+B	5,6	13,14	42,43	...
[S II] λ 6716/6731	N	5	13	44,45	Free

Note. For each line, N and B represent narrow ($\text{FWHM} \leq 1200 \text{ km s}^{-1}$) and broad ($\text{FWHM} \leq 10,000 \text{ km s}^{-1}$) Gaussian components. The Ly α through [Ne V] lines are treated with a broad component only when $S/N < 5$. The values in the Center, FWHM, and Flux columns represent independent fitting parameters such that identical values indicate that they are tied to each other. The Flux Ratio column denotes whether the doublets are treated with a fixed or free line ratio, and the value is the line ratio of the stronger doublet to the weaker.

the features at low S/N . We used the IDL-based package MPFIT (Markwardt 2009) to perform iterative least χ^2 fitting with a set of initial parameter values determined from the relative strengths of the features. The fit was improved by applying a 2.5σ Gaussian clipping (Wu et al. 2018) and masking some strong outlying values still left on the spectra (Section 2.2). Detailed prescriptions are described below, and Table 2 summarizes the broad/narrow nature of the selected lines and the independent/determined parameters.

For the rest-frame 3500–7000 Å fit, we assumed a power-law continuum and Gaussian emission lines for [O II] λ 3727, H γ , [O III] λ 4363, H β , [O III] λ 4959/5007, [O I] λ 6300, [N II] λ 6548/6583, H α , and [S II] λ 6716/6731. Traditionally, hydrogen Balmer lines in AGNs are fit by both broad and narrow components, with the dividing line between these components at $\text{FWHM} = 1000 \text{ km s}^{-1}$, while forbidden transitions are treated as narrow lines only. However, this standard approach is inappropriate for asymmetric, blueshifted, and broadened forbidden line profiles, as observed in some [O III] doublets and even for some [O II] and hydrogen Balmer lines in type 2 quasars (e.g., Zakamska & Greene 2014; Kang et al. 2017; Wu et al. 2018). These profiles are often broad, but instead of being broadened by the motions of the broad-line region clouds, they are thought to be broadened by emission from ionized gas outflowing from the AGN at $\sim 10^3 \text{ km s}^{-1}$ (Veilleux et al. 1994; Crenshaw & Kraemer 2000).

Independent of the origin of the broad-line components, we fit a single narrow ($\text{FWHM} \leq 1200 \text{ km s}^{-1}$) and a single broad ($\text{FWHM} \leq 10,000 \text{ km s}^{-1}$) Gaussian to the Balmer lines (H α , H β , H γ) and [O II], [O III] doublets.¹³ To benefit from multiple

lines being covered within the fitting range, we fix the line centers and widths by a single redshift and FWHM for all of the narrow components, and likewise for the broad hydrogen lines and [O II] with undetermined origin (see Section 4.5 for the interpretation), except for the narrow/broad [O III] components, where we further use separate redshifts and FWHMs to account for outflows. Exceptions include W2016–0041 (H β /H γ), where we removed the broad component, as the noise around a narrow line was fit without a clear detection. The [O III] λ 4363, [O I], [N II], and [S II] lines are weak and do not show any signs of deviation from a narrow profile; thus, they were fit with single narrow Gaussians.

We note that tying the Balmer line widths is a simplified assumption, since the broad H β line is empirically 10%–20% wider than broad H α (e.g., Jun et al. 2015). However, jointly constraining the line center and width is appropriate given the S/N of our data. Also, we allowed the narrow- and broad-line centers to be within -1000 to 1000 and -2000 to 1000 km s^{-1} of the systemic redshift (Section 4.1), respectively, to account for the blueshift/redshift of the broad component. We fix the [O III] doublet ratio to 2.98 (e.g., Storey & Zeippen 2000; Dimitrijević et al. 2007) and the [N II] doublet ratio to 2.96 (e.g., Greene & Ho 2005b; Wu et al. 2018) but leave the [S II] doublet ratio free, as it is less blended with other lines, and we can use this line ratio to estimate the electron density (see Section 4.4).

Next, we fit the rest-frame UV wavelengths separately in the 1150–2000 and 2000–3500 Å windows in order to better fit the continuum, which often shows a downturn at wavelengths shorter than 2000–3000 Å (e.g., W2026+0716 and W2042–3245; also, e.g., Jun & Im 2013 for quasars in general). We restricted the fitting range of two objects showing significant features in the continuum around C IV (W1719+0446 and W2042–3245). We fit a power-law continuum and Gaussian(s) for the Ly α , N V, C IV, and C III] lines within the 1150–2000 Å region and the Mg II and [Ne V] lines within the 2000–3500 Å region. As the targets have a relatively red rest-frame UV–optical color, the rest-UV emission lines are typically weaker than the rest-optical lines. Note that fitting a double Gaussian profile to a low- S/N line often overfits a weak, broad component indistinguishable from the noise, which stands out, as well-fit lines are consistently narrower. Thus, we only use double Gaussians (i.e., narrow and broad) to fit lines in the 1150–2000 or 2000–3500 Å regions with an $S/N \geq 5$ detection and a single Gaussian ($\text{FWHM} \leq 10,000 \text{ km s}^{-1}$) for the others.

In Figure 3, we plot the fits to the spectra for well-detected ($S/N \geq 3$) emission lines and list the line properties in Tables 3–5. The detection rates for the strongest lines, more than half detected, are 5/9 (Ly α), 9/11 ([O II]), 8/12 (H β), 11/12 ([O III]), and 8/8 (H α). The corresponding numbers for the weaker lines are 3/9 (N V), 1/9 (C IV), 1/10 (C III]), 3/10 (Mg II), 3/10 ([Ne V]), 0/11 (H γ), 4/8 ([O I]), 4/8 ([N II]), and 3/8 ([S II]). We focus on the stronger lines for the statistical analysis of the ionized gas outflows and broad-line kinematics and use $S/N \geq 5$ or ≥ 3 cuts depending on the parameter of interest.

4. Results and Discussion

4.1. Redshift

The first goal for the XSHOOTER observations was to identify undetermined redshifts and confirm the redshifts of

¹³ We loosen the narrow and broad line width constraints, as there are widths converging around $1000\text{--}1200 \text{ km s}^{-1}$ (Table 3), or the fit converges when the broad component is allowed to be narrower than 1000 km s^{-1} . When both components and the combined profile have $\text{FWHM} < 1200 \text{ km s}^{-1}$, we assume the total profile to be narrow.

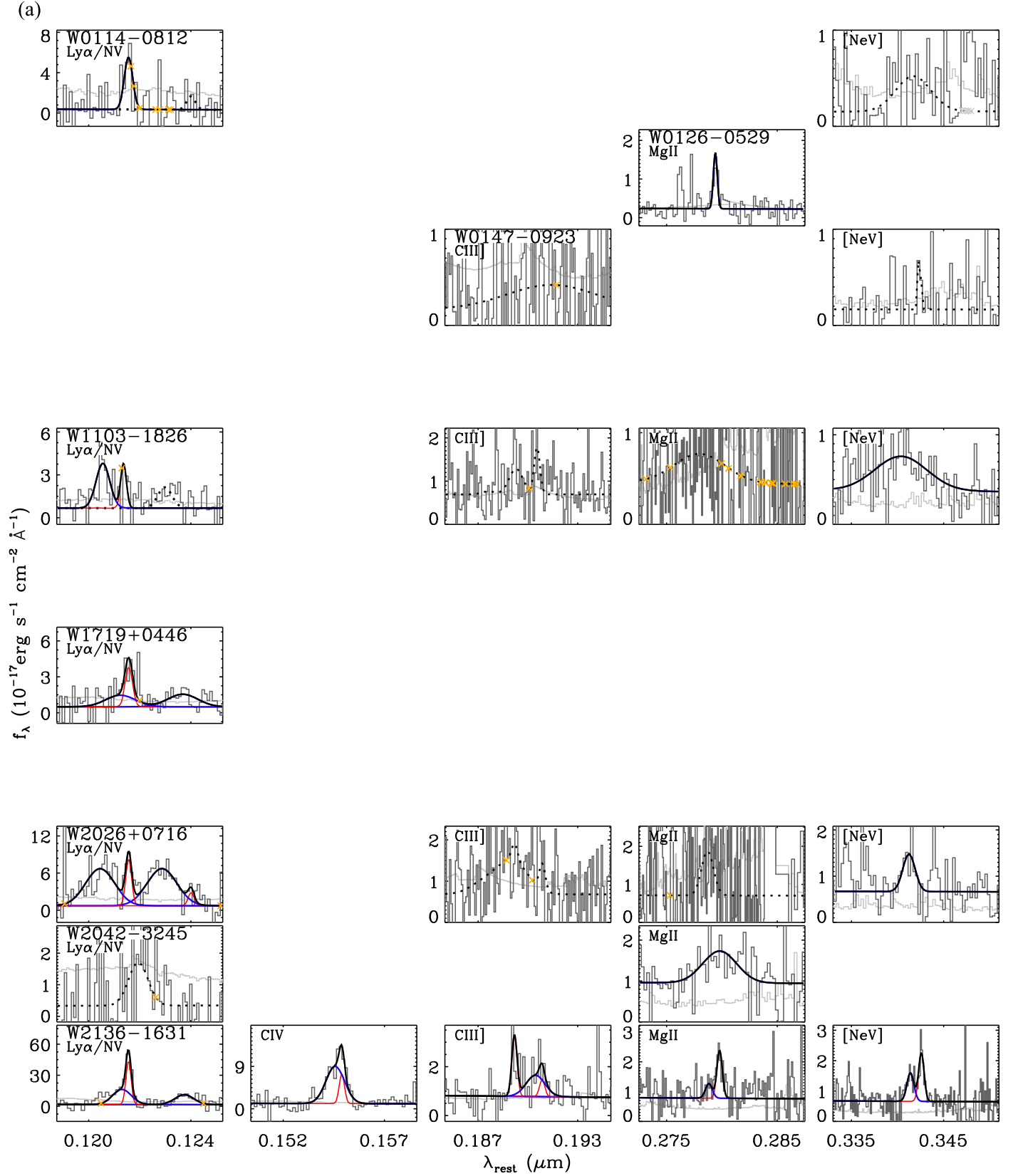


Figure 3. Model fit to the rest-frame, resolution-matched spectra of the sample, overplotted on the flux (black histogram) and uncertainty (gray histogram) spectra. The narrow (red) and broad (blue) components are highlighted. Wavelengths masked with strong telluric absorption or high sky background are marked (yellow crosses), and we only show the panels with detected lines (solid for $S/N \geq 3$ and dotted for $S/N \geq 2$). The wavelength limits for each panel are scaled to show $\pm 8000 \text{ km s}^{-1}$ from the panel center. (b) Continued from Figure 3, for the rest-optical spectra.

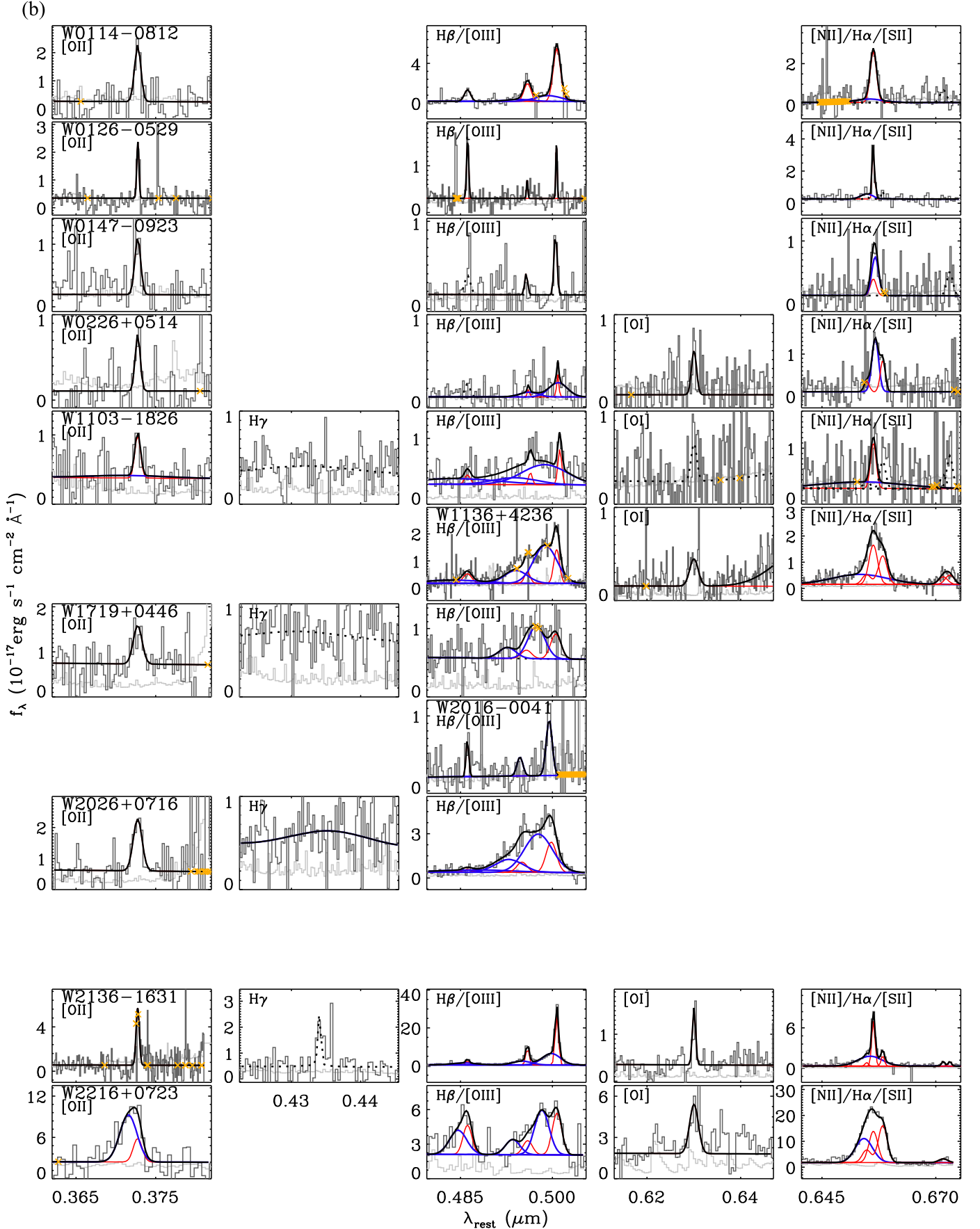


Figure 3. (Continued.)

Table 3
Rest-optical Emission Line Properties

Name	$\log L$ (erg s ⁻¹)	Δv (km s ⁻¹)	FWHM (km s ⁻¹)	σ (km s ⁻¹)	$\log L_{\text{bl}}$ (erg s ⁻¹)	Δv_{bl} (km s ⁻¹)	FWHM _{bl} (km s ⁻¹)	$\log L_{\text{nl}}$ (erg s ⁻¹)	Δv_{nl} (km s ⁻¹)	FWHM _{nl} (km s ⁻¹)
[O II]										
W0114-0812	43.81 ± 0.06	0 ± 25	735 ± 52	312 ± 22	... ± ± ± ...	43.81 ± 0.06	0 ± 25	735 ± 52
W0126-0529	42.37 ± 0.07	25 ± 17	250 ± 27	106 ± 12	... ± ± ± ...	42.37 ± 0.07	25 ± 17	250 ± 27
W0147-0923	43.51 ± 0.12	0 ± 80	686 ± 123	291 ± 52	... ± ± ± ...	43.51 ± 0.12	0 ± 80	686 ± 123
W0226+0514	43.36 ± 0.10	0 ± 57	599 ± 87	254 ± 37	... ± ± ± ...	43.36 ± 0.10	0 ± 57	599 ± 87
W1103-1826	43.72 ± 0.25	-23 ± 50	724 ± 104	662 ± 207	43.38 ± 0.52	-1122 ± 1130	10000 ± 38	43.45 ± 0.11	0 ± 67	676 ± 104
W1719+0446	43.79 ± 0.14	0 ± 138	1048 ± 247	445 ± 105	... ± ± ± ...	43.79 ± 0.14	0 ± 138	1048 ± 247
W2026+0716	44.10 ± 0.08	0 ± 86	1049 ± 138	446 ± 59	... ± ± ± ...	44.10 ± 0.08	0 ± 86	1049 ± 138
W2136-1631	43.68 ± 0.05	-1 ± 3	379 ± 7	161 ± 3	... ± ± ± ...	43.68 ± 0.05	-1 ± 3	379 ± 7
W2216+0723	44.65 ± 0.11	-751 ± 49	2306 ± 375	890 ± 99	44.55 ± 0.11	-944 ± 215	2056 ± 299	43.96 ± 0.36	0 ± 65	1054 ± 71
H β										
W0114-0812	43.69 ± 0.06	0 ± 24	735 ± 52	312 ± 22	... ± ± ± ...	43.69 ± 0.06	0 ± 24	735 ± 52
W0126-0529	42.25 ± 0.08	25 ± 16	250 ± 27	106 ± 12	... ± ± ± ...	42.25 ± 0.08	25 ± 16	250 ± 27
W1103-1826	43.92 ± 0.10	-522 ± 53	1025 ± 115	1582 ± 4	43.88 ± 0.11	-1122 ± 1130	10000 ± 38	42.93 ± 0.23	0 ± 67	676 ± 104
W1136+4236	43.95 ± 0.06	-424 ± 17	1259 ± 41	1548 ± 36	43.79 ± 0.08	-1360 ± 167	6533 ± 324	43.45 ± 0.06	0 ± 24	1022 ± 41
W2016-0041	43.19 ± 0.16	0 ± 55	310 ± 84	131 ± 36	... ± ± ± ...	43.19 ± 0.16	0 ± 55	310 ± 84
W2026+0716	44.15 ± 0.15	545 ± 110	1880 ± 278	2573 ± 136	44.09 ± 0.17	986 ± 61	8726 ± 2303	43.26 ± 0.23	0 ± 86	1049 ± 138
W2136-1631	44.07 ± 0.04	-216 ± 3	841 ± 18	963 ± 14	43.97 ± 0.04	-334 ± 42	2870 ± 93	43.42 ± 0.05	0 ± 3	379 ± 7
W2216+0723	44.36 ± 0.10	-582 ± 59	1865 ± 243	870 ± 83	44.15 ± 0.13	-944 ± 215	2056 ± 299	43.95 ± 0.17	0 ± 64	1054 ± 71
[O III]										
W0114-0812	44.56 ± 0.04	-158 ± 17	889 ± 30	695 ± 48	44.00 ± 0.12	-815 ± 210	2920 ± 335	44.41 ± 0.02	20 ± 20	827 ± 29
W0126-0529	42.06 ± 0.13	-1 ± 19	148 ± 39	63 ± 17	... ± ± ± ...	42.06 ± 0.13	-1 ± 19	148 ± 39
W0147-0923	43.24 ± 0.09	-108 ± 59	333 ± 55	142 ± 23	... ± ± ± ...	43.24 ± 0.09	-108 ± 59	333 ± 55
W0226+0514	43.48 ± 0.15	125 ± 41	440 ± 110	603 ± 35	43.40 ± 0.13	145 ± 248	2111 ± 568	42.68 ± 0.24	112 ± 69	244 ± 104
W1103-1826	44.21 ± 0.06	-891 ± 74	1788 ± 194	1980 ± 170	44.15 ± 0.09	-1172 ± 266	5211 ± 662	43.32 ± 0.09	309 ± 56	432 ± 73
W1136+4236	44.57 ± 0.02	-905 ± 17	2362 ± 82	1116 ± 36	44.48 ± 0.03	-1110 ± 56	2662 ± 96	43.83 ± 0.04	8 ± 25	668 ± 51
W1719+0446	44.10 ± 0.10	-1359 ± 141	1326 ± 313	1151 ± 123	43.94 ± 0.45	-1968 ± 97	1988 ± 412	43.61 ± 0.18	-82 ± 184	1189 ± 369
W2016-0041	43.71 ± 0.14	-721 ± 102	691 ± 192	293 ± 81	43.71 ± 0.28	-721 ± 102	691 ± 192	... ± ± ± ...
W2026+0716	45.01 ± 0.02	-1495 ± 61	3000 ± 107	1338 ± 41	44.90 ± 0.04	-1785 ± 85	3227 ± 121	44.37 ± 0.03	-519 ± 69	1200 ± 0
W2136-1631	44.87 ± 0.01	-215 ± 3	609 ± 6	613 ± 7	44.61 ± 0.01	-515 ± 21	2089 ± 32	44.53 ± 0.01	18 ± 3	387 ± 4
W2216+0723	44.55 ± 0.07	-882 ± 47	2811 ± 1096	960 ± 97	44.34 ± 0.10	-1443 ± 164	1690 ± 348	44.13 ± 0.12	38 ± 126	1099 ± 214
H α										
W0114-0812	44.25 ± 0.11	-60 ± 37	771 ± 54	568 ± 193	43.59 ± 0.45	-430 ± 485	3074 ± 1146	44.15 ± 0.05	-1 ± 24	735 ± 52
W0126-0529	43.03 ± 0.11	-188 ± 130	890 ± 436	461 ± 230	42.52 ± 0.31	-650 ± 396	1371 ± 767	42.86 ± 0.06	24 ± 16	250 ± 27
W0147-0923	43.79 ± 1.08	131 ± 75	808 ± 216	339 ± 73	43.65 ± 1.05	179 ± 429	805 ± 212	43.22 ± 2.82	-1 ± 80	686 ± 123
W0226+0514	44.00 ± 0.09	188 ± 63	780 ± 140	331 ± 60	44.00 ± 0.09	188 ± 63	780 ± 140	... ± ± ± ...
W1103-1826	44.33 ± 0.14	-49 ± 47	760 ± 104	902 ± 59	44.16 ± 0.20	-1122 ± 1130	10000 ± 38	43.84 ± 0.12	0 ± 67	676 ± 104
W1136+4236	44.63 ± 0.02	-335 ± 23	1194 ± 41	1401 ± 23	44.42 ± 0.03	-1360 ± 167	6533 ± 324	44.21 ± 0.02	0 ± 23	1022 ± 41
W2136-1631	44.46 ± 0.01	-69 ± 3	467 ± 7	560 ± 6	44.25 ± 0.02	-335 ± 42	2870 ± 93	44.05 ± 0.01	-1 ± 4	379 ± 7
W2216+0723	45.15 ± 0.06	-565 ± 64	1791 ± 221	866 ± 93	44.92 ± 0.09	-944 ± 215	2056 ± 299	44.75 ± 0.09	0 ± 65	1054 ± 71

Note. Here L is the luminosity, Δv is the offset (luminosity-weighted first moment) for the total profile or Gaussian center for each broad/narrow component with respect to the systemic redshift, and σ is the line dispersion (luminosity-weighted second moment). Subscripts “bl” and “nl” indicate broad-line and narrow-line, respectively. The properties of the broad and narrow components are denoted with subscripts. We show only the fitted values for detected lines ($S/N \geq 3$ from the total profile), and values from a component with no contribution to the model are left blank.

Table 4
Rest Far-UV Emission Line Properties

Name	$\log L$ (erg s ⁻¹)	Δv (km s ⁻¹)	FWHM (km s ⁻¹)	σ (km s ⁻¹)	$\log L_{\text{bl}}$ (erg s ⁻¹)	Δv_{bl} (km s ⁻¹)	FWHM _{bl} (km s ⁻¹)	$\log L_{\text{nl}}$ (erg s ⁻¹)	Δv_{nl} (km s ⁻¹)	FWHM _{nl} (km s ⁻¹)
Lyα										
W0114-0812	43.85 \pm 0.20	56 \pm 134	960 \pm 309	408 \pm 131	43.85 \pm 0.20	56 \pm 134	960 \pm 309	... \pm \pm \pm ...
W1103-1826	44.18 \pm 0.12	-1827 \pm 94	3120 \pm 1072	1082 \pm 103	44.02 \pm 0.14	-2415 \pm 158	1571 \pm 368	43.64 \pm 0.23	-421 \pm 109	653 \pm 236
W1719+0446	44.13 \pm 0.19	-247 \pm 97	1002 \pm 279	988 \pm 179	43.87 \pm 0.30	-716 \pm 542	3371 \pm 1002	43.80 \pm 0.20	91 \pm 144	843 \pm 290
W2026+0716	44.76 \pm 0.06	-2119 \pm 74	2432 \pm 250	1689 \pm 110	44.66 \pm 0.07	-2676 \pm 155	3334 \pm 368	44.06 \pm 0.13	81 \pm 89	667 \pm 164
W2136-1631	44.64 \pm 0.07	-245 \pm 8	727 \pm 71	682 \pm 37	44.38 \pm 0.10	-574 \pm 104	2102 \pm 189	44.30 \pm 0.08	58 \pm 27	592 \pm 75
N v										
W1719+0446	43.91 \pm 0.19	-716 \pm 541	3371 \pm 1002	1431 \pm 425	43.91 \pm 0.19	-716 \pm 541	3371 \pm 1002	... \pm \pm \pm ...
W2026+0716	44.70 \pm 0.06	-2495 \pm 76	4406 \pm 521	1534 \pm 152	44.67 \pm 0.06	-2677 \pm 155	3334 \pm 368	43.52 \pm 0.29	80 \pm 88	667 \pm 164
W2136-1631	44.21 \pm 0.11	-576 \pm 104	2102 \pm 189	893 \pm 80	44.21 \pm 0.11	-576 \pm 104	2102 \pm 189	... \pm \pm \pm ...
C iv										
W2136-1631	44.31 \pm 0.05	-460 \pm 5	1621 \pm 131	849 \pm 67	44.22 \pm 0.06	-576 \pm 103	2101 \pm 189	43.57 \pm 0.12	57 \pm 27	589 \pm 75
C iii]										
W2136-1631	43.44 \pm 0.16	-461 \pm 8	1629 \pm 132	850 \pm 38	43.35 \pm 0.18	-575 \pm 104	2101 \pm 189	42.70 \pm 0.40	56 \pm 28	589 \pm 75

Note. The format follows that of Table 3, except that we show single-component ($\text{FWHM} \leq 10,000 \text{ km s}^{-1}$) models from regions with line S/N < 5 (using Ly α for 1150–2000 Å and Mg II for 2000–3500 Å) along with the broad-component models for objects with S/N ≥ 5 . By construction, some single components show narrow ($\text{FWHM} \leq 1200 \text{ km s}^{-1}$) widths.

Table 5
Rest Near-UV Emission Line Properties

Name	$\log L$ (erg s ⁻¹)	Δv (km s ⁻¹)	FWHM (km s ⁻¹)	σ (km s ⁻¹)	$\log L_{\text{bl}}$ (erg s ⁻¹)	Δv_{bl} (km s ⁻¹)	FWHM _{bl} (km s ⁻¹)	$\log L_{\text{nl}}$ (erg s ⁻¹)	Δv_{nl} (km s ⁻¹)	FWHM _{nl} (km s ⁻¹)
Mg II										
W0126–0529	42.33 ± 0.15	−416 ± 50	439 ± 114	185 ± 49	42.33 ± 0.15	−416 ± 50	439 ± 114	... ± ± ± ...
W2042–3245	44.35 ± 0.16	0 ± 618	3865 ± 1085	1641 ± 461	44.35 ± 0.16	0 ± 618	3865 ± 1085	... ± ± ± ...
W2136–1631	43.39 ± 0.09	−296 ± 55	624 ± 74	540 ± 49	42.84 ± 0.20	−1050 ± 70	776 ± 177	43.25 ± 0.09	−10 ± 33	608 ± 80
[Ne V]										
W1103–1826	44.13 ± 0.11	−1943 ± 47	5853 ± 1132	2485 ± 481	44.13 ± 0.11	−1943 ± 47	5853 ± 1132	... ± ± ± ...
W2026+0716	43.86 ± 0.16	−1179 ± 160	1373 ± 377	583 ± 160	43.86 ± 0.16	−1179 ± 160	1373 ± 377	... ± ± ± ...
W2136–1631	43.58 ± 0.07	−507 ± 39	1535 ± 1059	588 ± 33	43.21 ± 0.12	−1050 ± 69	777 ± 177	43.33 ± 0.07	−9 ± 33	609 ± 80

Note. The format follows that of Table 3, with the same exception as Table 4.

some sources with existing but uncertain optical spectroscopy (P. R. M. Eisenhardt et al. 2019, in preparation). We define quality “A” and “B” redshifts as those derived from sources with two or more lines with $S/N \geq 5$ and ≥ 2 , respectively. The systemic redshift is determined by the peak of the model fit around the prominent emission lines (from the common narrow component center of the $H\alpha$, $H\beta$, and $[O II]$ lines and that of $Mg II$ and $[Ne V]$), which should suffer less from systematic blueshifts (C IV) or blending issues ($Ly\alpha$, N V, C III), $H\gamma$). We combined the UV and optical redshifts from $S/N \geq 3$ detections and performed error-weighted averaging to calculate the systemic redshifts and uncertainty values. Comparing the systemic (redshift with median uncertainty of 0.00047) to the individual redshifts from the total profile of the stronger lines, we find that the latter lies mostly within three times its uncertainty to the systemic from the $[O II]$ line with $S/N \geq 3$ (8/9) but not from the $H\beta$ (3/8), $[O III]$ (1/11), and $H\alpha$ (3/8) lines, where they often show clear blueshifts (Sections 4.4 and 4.5).

Out of the 10 XSHOOTER spectra, we determine two new redshifts (quality “A” for W0114–0812 and quality “B” for W2016–0041) and study eight with existing values (P. R. M. Eisenhardt et al., in preparation; including two redshifts added in Tsai et al. 2015). Six of these match within 1% to existing values (all quality “A” redshifts). However, two differ drastically: quality “A” $z = 0.8301$ for W0126–0529, previously $z = 2.937$, and quality “B” $z = 2.958$ for W2042–3245¹⁴, previously $z = 3.963$. The two mismatches occur for redshifts previously determined from Gemini/GMOS observed-frame 4000–6500 Å spectra (Tsai et al. 2015). Both were quality “B” redshifts, derived by the detection but uncertain identification of a single feature. The broadband VLT spectra emphasize the importance of multiple line detections for confident redshift determinations, although our quality “B” redshifts could still be biased by noise, and we remove those sources from further analysis. As a side note, the two redshifts (W1136+4236 and W2216+0723) from Wu et al. (2018) were not flagged in their work but are both quality “A” by our definition, showing a clear detection of multiple lines.

4.2. Spectral Classification

We can obtain spectroscopic classifications of our targets, such as the Seyfert type¹⁵ (e.g., Osterbrock 1981), Baldwin, Phillips & Terlevich (BPT) diagram (e.g., Baldwin et al. 1981), $[O II]$ – $[O III]$ line ratio (e.g., Ferland & Osterbrock 1986), and $H\alpha$ -to- $H\beta$ ratio (e.g., Osterbrock 1989), to better differentiate between the AGN and star-forming properties of Hot DOGs. According to the narrow-to-broad-line flux ratios for Balmer lines (assuming the broad lines come from the broad-line region, not from outflows), all targets with sufficient emission line $S/N (\geq 5)$ in $H\alpha$ ($N = 8$) or $H\beta$ ($N = 4$) show a clear narrow component with no pure type 1 (broad-line-dominated) classification. We calculate the Seyfert types using the total $[O III]/H\beta$ ratio and detectability of broad Balmer lines (Winkler 1992) using $S/N \geq 3$ detections (and 3σ upper limits) for the $[O III]/H\beta$ ratio and $S/N \geq 5$ detections for the detectability of broad Balmer lines. The Seyfert types shown in

Table 6
Seyfert Type

Name	Seyfert $H\beta/[O III]$	Broad $H\beta$	Broad $H\alpha$	Combined
W0114–0812	≥ 1.8	No	Yes	1.9
W0126–0529	1.2–1.5	No	Yes	...
W0147–0923	≥ 1.5	...	No	2.0
W0226+0514	≥ 1.5	...	No	2.0
W1103–1826	1.5	...	Yes	1.5
W1136+4236	≥ 1.8	...	Yes	1.8–1.9
W1719+0446	≥ 1.2	≥ 1.2
W2026+0716	≥ 1.8	≥ 1.8
W2136–1631	≥ 1.8	Yes	Yes	1.8
W2216+0723	1.5	Yes	Yes	1.5

Note. The Seyfert types are determined by the $H\beta/[O III]$ ratio (types 1.0, 1.2, 1.5, and ≥ 1.8 , divided by $H\beta/[O III]$ ratios of 5, 2, and 1/3) and the detectability of broad Balmer lines (≤ 1.8 if $H\beta$ and $H\alpha$ are present, 1.9 if only $H\alpha$ is, and 2.0 if both are absent), following Winkler (1992). Ranges in the values are given by taking into account the uncertainty in the $H\beta/[O III]$ ratio, the 3σ upper limit on $H\beta$ flux ($[O III]$ instead of $H\beta$ for W1719+0446 due to complete nondetection), and the absence of broad Balmer line detectability at $S/N < 5$.

Table 6 range from type 1.5 (intermediate $H\beta$ to $[O III]$, 2/8) to type 1.8 and higher (weak $H\beta$ to $[O III]$, 6/8), apart from the undetermined type for W0126–0529 (which turns out not to be an AGN; Table 7) and a loosely determined type for W1719+0446 (type ≥ 1.2). Our type 1 fraction (2/8 counting up to type 1.5, but 3–5/8 when including type 1.8–1.9 sources as type 1), together with a majority of single broad Balmer line FWHM values of $\lesssim 3000 \text{ km s}^{-1}$ in Table 3, are marginally different from other red quasar spectra in the literature, which show type 1 fractions of $\gtrsim 50\%$ – 57% (e.g., Glikman et al. 2012; Banerji et al. 2015; Ross et al. 2015) with a single broad-line FWHM $\gtrsim 3000 \text{ km s}^{-1}$. This difference likely arises because our targets have higher extinction (Section 2.1) and hence are obscuring more of the broad-line region.

Using the narrow-line ($FWHM < 1200 \text{ km s}^{-1}$) ratios with $S/N \geq 3$ detections or 3σ upper limits, we plot the $[N II]$, $[S II]$, and $[O I]$ BPT diagrams in Figure 4. There are eight values in each panel and two lower limits on $[O III]/H\beta$ outside the plots based on the absence of $[N II]/H\alpha$ (W1719+0446, W2026+0716). For $E(B-V) \lesssim 1$ (e.g., Table 8) and a Milky way extinction curve, the $[N II]/H\alpha$, $[S II]/H\alpha$, $[O I]/H\alpha$, and $[O III]/H\beta$ change by less than 0.004, 0.03, -0.06 , and 0.06 dex if corrected for extinction, which is within the measurement uncertainties. We list each and the combined classifications based on the most overlaps in Table 7. Combined, seven are BPT AGNs, two are unconstrained (W0147–0923 and W1719+0446), and the remaining object is star-forming (W0126–0529). The latter source, the lowest-redshift galaxy in our sample, is not considered in the following when deducing and discussing the AGN properties of our targets. Considering the $[S II] \lambda 6716$, 6731 and $[O I] \lambda 6300$ BPT diagrams, the remaining targets always favor the so-called Seyfert region of these diagrams over the LINER region, implying that Hot DOGs have a strong ionization source from the AGN.

We independently check for signs of star formation activity in our sample using the $[O II]/[O III]$ line ratio (e.g., Ho 2005; Kim et al. 2006), as the $[O II]$ emission usually originates from star formation rather than the AGN activity, and conversely for

¹⁴ We have $S/N = 2.0$ ($Ly\alpha$), 1.8 (C IV), and 4.2 ($Mg II$) from XSHOOTER, but with weak S/N , this is still classified as quality “B”.

¹⁵ Throughout, we use the classic term Seyfert to distinguish from H II regions or LINERs, but we note that the luminosities of Hot DOGs fall into the quasar regime.

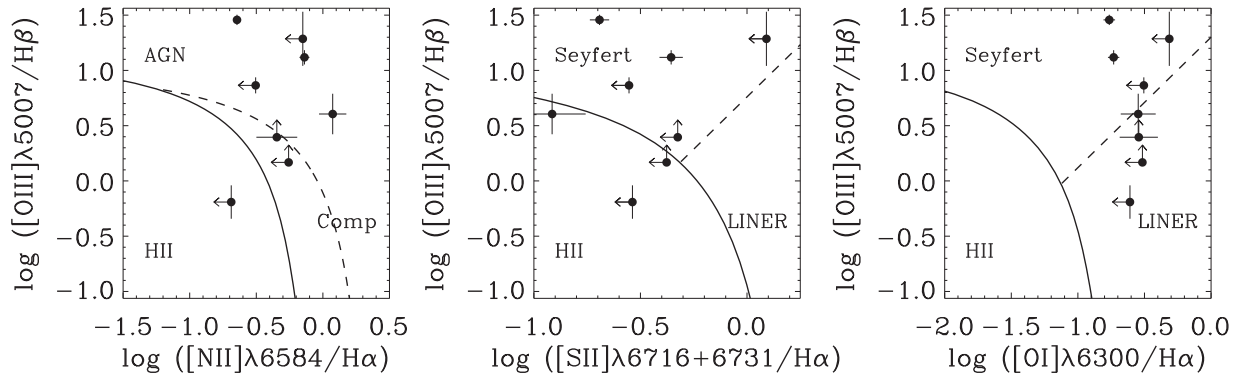


Figure 4. The BPT diagrams of the sample. Black dots are the line ratios derived from the narrow-line fluxes with $S/N \geq 3$, and arrows indicate the ratios based on 3σ upper limits. Solid lines denote the dividing lines between star-forming and AGN ratios for all panels (Kewley et al. 2001). The dashed line is between pure AGN and composite star-forming and AGN ratios for the left panel (Kauffmann et al. 2003) and Seyfert and LINER-type AGN ratios for the middle and right panels (Kewley et al. 2006). The axes are scaled to follow the observed distribution of typical AGNs (e.g., Kewley et al. 2006).

Table 7
BPT Classification

Name	BPT Ratios [O III]/H β	[N II]/H α	[S II]/H α	[O I]/H α	BPT Classification [N II]	[S II]	[O I]	Combined
W0114–0812	0.86 ± 0.07	< -0.50	< -0.55	< -0.50	AGN/H II	Sy	Sy	Sy
W0126–0529	-0.19 ± 0.15	< -0.69	< -0.54	< -0.61	H II	H II	H II/LI	H II
W0147–0923	> 0.17	< -0.26	< -0.38	< -0.52	Any	H II/Sy	Any	Any
W0226+0514	> 0.40	-0.35 ± 0.15	< -0.32	-0.54 ± 0.14	Comp/AGN	H II/Sy	Sy/LI	Sy
W1103–1826	1.29 ± 0.24	< -0.15	< 0.09	< -0.31	AGN	Sy	Sy	Sy
W1136+4236	1.12 ± 0.06	-0.14 ± 0.04	-0.36 ± 0.05	-0.73 ± 0.04	AGN	Sy	Sy	Sy
W1719+0446	> -0.33
W2026+0716	> 1.56	AGN	Sy	Sy	Sy
W2136–1631	1.46 ± 0.05	-0.64 ± 0.03	-0.69 ± 0.05	-0.76 ± 0.04	AGN	Sy	Sy	Sy
W2216+0723	0.60 ± 0.18	0.07 ± 0.10	-0.91 ± 0.16	-0.55 ± 0.13	AGN	H II/Sy	Sy/LI	Sy

Note. The BPT types composite, Seyfert, and LINER are abbreviated as Comp, Sy, and LI. Empty values correspond to the line not being covered. Upper/lower limits are based on 3σ detection limits unless the line is completely undetected, where we use 3σ limits for H α instead of [N II] or [O I] for W0114–0812 and [O III] instead of H β for W1719+0446. The combined BPT classification is determined by the majority of the individual classifications.

[O III]. The [O II]/[O III] ratio values based on $S/N \geq 3$ detections are listed in Table 8. Indeed, out of eight objects with both BPT classification and [O II]/[O III] ratio values, three that are classified exclusively as AGNs in all three BPT diagrams have [O II]/[O III] values of 0.1–0.4, and five with at least one potential H II BPT classification have [O II]/[O III] values of 0.2–2.6. This is consistent with pure AGNs on the BPT diagrams showing stronger [O III] to those with potentially mixed star formation with stronger [O II]. The diverse range of [O II]/[O III] ratios is in line with a combination of AGN and star-forming galaxy templates explaining the photometric SEDs of Hot DOGs (e.g., Assef et al. 2015), but we caution against any conclusive interpretation of the AGN/star-forming nature of the oxygen lines, as the [O II] line could also originate from the AGN activity (e.g., Yan et al. 2006; Maddox 2018; Section 4.5). Overall, the majority (7/8) of Hot DOGs are best explained as non-LINER AGNs on the BPT diagrams, and AGN activity dominates star formation in both the BPT and [O II]/[O III] diagnostics.

4.3. Extinction Measures

We next investigate the level of obscuration within the narrow-line region using the Balmer decrements (narrow

H α /H β) listed in Table 8. Observationally, Kim et al. (2006) showed that type 1 AGNs generally have Balmer decrements close to the expected value, with a distribution sharply peaked at H α /H β = 3.3, while Zakamska et al. (2003) showed that type 2 AGNs have higher values, with an average of 4.1 measured from their composite spectrum. Most (7/8) of our sources show Balmer decrements $\gtrsim 4$, indicating large amounts of dust obscuration. The translated $E(B-V)$ values assuming the intrinsic Balmer decrements of 3.1 expected for AGN narrow-line regions (e.g., Osterbrock 1989) lie mostly around 0.3–0.7 mag, which is not only an order of magnitude higher than the type 1 AGN values (0.06 mag) in Kim et al. (2006) but also up to several times higher than that of the type 2 quasars at various redshifts (~ 0.3 mag; Zakamska et al. 2003; Greene et al. 2014). Interestingly, the $E(B-V)$ values from the broadband SED fitting (3–20 mag; Table 1) are another order of magnitude larger than the values inferred from the Balmer decrements (Table 8). This has already been seen (Zakamska et al. 2003, 2005; Greene et al. 2014) from similar measurements of candidate type 2 quasars, altogether suggesting a dense, stratified distribution of dust between the compact accretion disk and the extended narrow-line region in quasars. This is also consistent with significant amounts of scattered

Table 8
Line Ratios and EWs

Name	[O II]/[O III]	H α /H β	$E(B-V)$ (mag)	EW _[O III] (Å)
W0114–0812	0.23 \pm 0.04	2.85 \pm 0.51	−0.09 \pm 0.18	259.1 \pm 59.8
W0126–0529	2.62 \pm 0.90	4.06 \pm 0.94	...	4.6 \pm 0.6
W0147–0923	2.47 \pm 0.84	>5.23	>0.53	11.1 \pm 2.1
W0226+0514	1.00 \pm 0.35	>8.32	>1.00	25.8 \pm 7.5
W1103–1826	0.42 \pm 0.25	8.12 \pm 4.86	0.98 \pm 0.61	43.8 \pm 6.7
W1136+4236	...	5.79 \pm 0.84	0.63 \pm 0.15	190.9 \pm 29.2
W1719+0446	0.64 \pm 0.50	17.5 \pm 2.9
W2026+0716	0.16 \pm 0.03	207.1 \pm 54.6
W2136–1631	0.08 \pm 0.01	4.29 \pm 0.47	0.33 \pm 0.11	384.5 \pm 32.0
W2216+0723	1.63 \pm 0.51	6.42 \pm 2.78	0.74 \pm 0.44	36.0 \pm 4.2

Note. Lower limits correspond to 3σ upper limits, and empty values indicate that the line is not being covered. The $E(B-V)$ values are determined from the measured narrow H α /H β values assuming an intrinsic Balmer decrement of 3.1, except for W0126–0529 being a BPT non-AGN.

continuum light from unobscured lines of sight in some Hot DOGs or extremely red quasars (e.g., Assef et al. 2016; Hamann et al. 2017).

Hot DOGs, therefore, seem to require not only a dense source of extinction interior to the narrow-line region but also an extended distribution of gas or dust outside it. The overall dust temperature of Hot DOGs (50–120 K; e.g., Wu et al. 2012; Bridge et al. 2013) is marginally higher than that of starburst galaxies, implying that the dust may be associated with the AGN activity. One possibility is to consider host galaxy dust (e.g., Rigby et al. 2006; Polletta et al. 2008). As favored by merger-driven quasar fueling models and observations of Hot DOGs (e.g., Hopkins et al. 2008; Fan et al. 2016; Farrah et al. 2017), the obscured starburst galaxy will receive feedback from the quasar activity and become unobscured (see also Buchner & Bauer 2017; Gobat et al. 2018 for discussion of how the gas content in $z \sim 2$ galaxies is higher than in local galaxies). We investigate whether the kiloparsec-scale obscuration is responsible for the reddening by estimating the spatial extent of the narrow-line region. We use the narrow-line region size–luminosity ($R_{\text{NLR}}-L_{[\text{O III}]}$) relation at extinction-uncorrected $L_{[\text{O III}]} \sim 10^{43.5-45} \text{ erg s}^{-1}$. This reaches the upper limit of ~ 10 kpc extrapolated from lower luminosities (e.g., Husemann et al. 2013; Hainline et al. 2014; Liu et al. 2014; Storch-Bergmann et al. 2018), comparable to or even larger than the size of the entire host galaxy. Thus, the extinction measured from the narrow-line region is more likely coming from the host galaxy, rather than from the central AGN.

Independent of the Balmer decrement–based $E(B-V)$ estimates, we list the extinction-uncorrected, spectroscopically derived [O III] rest-frame equivalent width (EW) values in Table 8. We compare the EW_[O III] values for Hot DOGs to type 1 and 2 quasars at matched luminosities ($L_{[\text{O III}]} \gtrsim 10^{43.5} \text{ erg s}^{-1}$ from Greene et al. 2014; $L_{5100} \gtrsim 10^{46.5} \text{ erg s}^{-1}$ from Shen 2016). It appears that there is a large discrepancy in the observed values; the type 1 EW_[O III] values are ~ 100 Å in Greene et al. (2014), as opposed to ~ 10 Å in Shen (2016). However, Shen (2016) noted the anticorrelation between EW_[O III] and L_{5100} ([O III] Baldwin effect; e.g., Baldwin 1977; Brotherton 1996), and as the data points in Greene et al. (2014) are from $L_{5100} \lesssim 10^{46} \text{ erg s}^{-1}$ quasars from Shen et al. (2011), we use the value of 10 Å in Shen (2016) as a reference. Hot DOGs with a non-H II BPT classification have EW_[O III] values around 10–400 Å (median = 44 Å), with a corresponding $E(B-V)$ between the

lines of sight through the accretion disk and the [O III] region of 0.03–1.14 mag (median 0.46 mag), assuming a Milky Way extinction curve. Note that we expect the intrinsic EW_[O III] values (and thus the inferred extinction values) to be higher than measured, since these heavily obscured AGNs are expected to have nonnegligible host galaxy contributions to their continuum emission.

4.4. Ionized [O III] Gas Outflows

In Figure 5, we plot model profiles of the strongest lines, [O II], H β /[O III], and H α , with their broad and narrow components highlighted. It is evident that most of the sample displays broadened or blueshifted [O III] indicative of ionized gas outflows, often modeled by biconical motions where the blue wing is less affected by obscuration than the red, leading to an asymmetric line profile (e.g., Crenshaw et al. 2010; Zakamska & Greene 2014; Bae & Woo 2016). To quantify the presence of outflows as clear nongravitational motion to our line of sight, we first require the presence of a broad [O III] component¹⁶ with $\sigma_{[\text{O III}], \text{broad}} > 400 \text{ km s}^{-1}$, to distinguish potential broadening by even the most massive galaxy potential. We also place an S/N ≥ 5 requirement on the [O III] line to enable robust separation of the broad component from the narrow component (as we did in Section 4.2), since line modeling is susceptible to noise at low S/N. The fraction of [O III] outflows is 8/9.

It is well known that outflows traced by [O III] line widths of $\sigma_{[\text{O III}], \text{broad}} > 400 \text{ km s}^{-1}$ are prevalent in average luminosity, type 1/2 quasars from the Sloan Digital Sky Survey (SDSS; e.g., Mullaney et al. 2013; Woo et al. 2016; Rakshit & Woo 2018), but we test whether the [O III] kinematics of Hot DOGs indicate higher $\sigma_{[\text{O III}], \text{broad}}$ values at their high luminosities. In Figure 6, we plot the broad [O III] line width, shift to the systemic redshift as a function of the observed (extinction-uncorrected) total [O III] luminosity for our targets, and compare them to other quasars in the literature. Among $L_{[\text{O III}]} > 10^{42} \text{ erg s}^{-1}$ quasars in the figure, 74%–79% have $\sigma_{[\text{O III}], \text{broad}} > 400 \text{ km s}^{-1}$, consistent with the majority of local AGNs showing outflows irrespective of type at $L_{[\text{O III}]} > 10^{42} \text{ erg s}^{-1}$ (e.g., Woo et al. 2016; Rakshit & Woo 2018). However, the eight Hot DOGs with [O III]

¹⁶ When we refer to Δv or σ of a Gaussian component ($\Delta v_{\text{broad/narrow}}$, $\sigma_{\text{broad/narrow}}$), it is directly converted as the model center and FWHM/2.355, respectively, whereas those of the total profile (Δv_{total} , σ_{total}) are calculated as the luminosity-weighted first or second moments of the model unless specified otherwise.

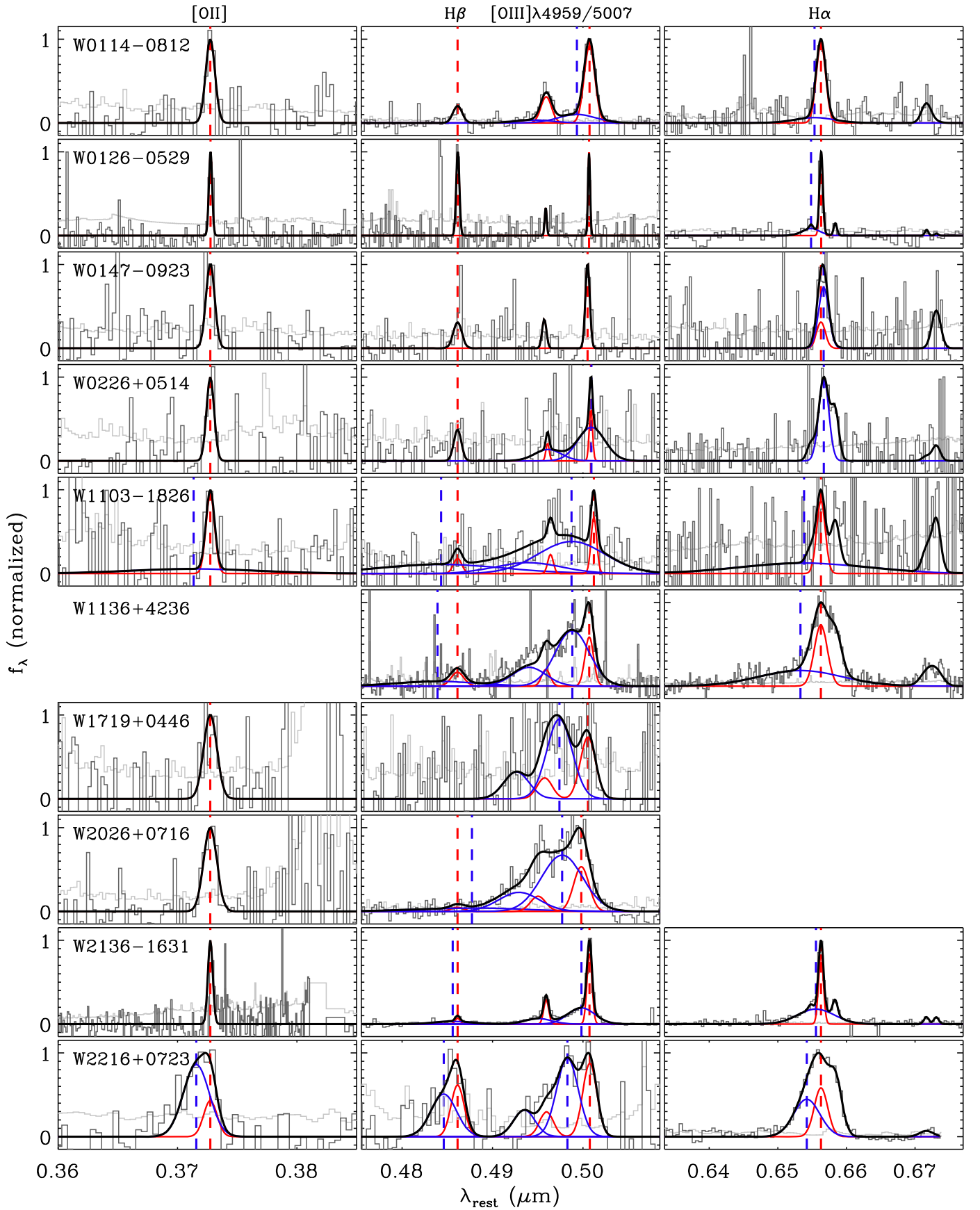


Figure 5. Model fit to the [O II], H β /[O III], and H α regions revisited. The format follows that of Figure 3, with additional red and blue vertical dashed lines indicating the center of the narrow and broad model components, respectively. The panels are scaled to show $\pm 10,000 \text{ km s}^{-1}$ from their centers.

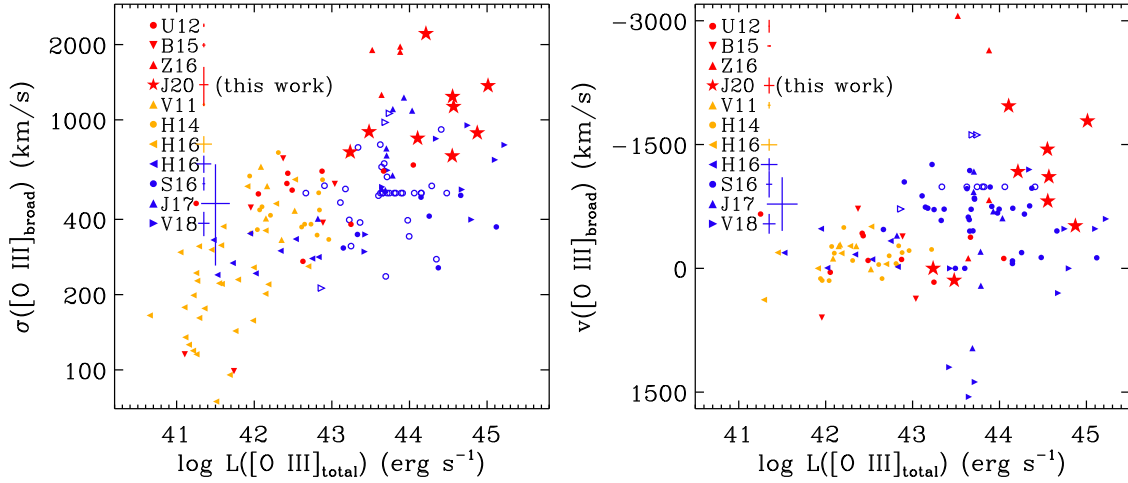


Figure 6. Broad [O III] width (σ , from FWHM/2.355) offset against observed (extinction-uncorrected) total [O III] luminosity. Our sample (red stars) is plotted together with literature data of type 1 (blue), type 2 (yellow), and obscured (red) quasars. We limit the data to those fit by a single narrow and a broad model decomposition of the [O III], keeping the narrow line width when the broad is absent. Open symbols are those where the best-fit model parameters are on their fitting boundary (S16; V18) or the total (broad+narrow) σ values for objects with $\sigma_{\text{total}} > \sigma_{\text{broad}}$ (S16). When uncertainties are available, only the data with uncertainties in the [O III] luminosity smaller than 20% and width smaller than 100% are plotted. Median uncertainties for each sample are shown when available, with the σ uncertainties scaled to when $\sigma_{[\text{O III}],\text{broad}} = 800 \text{ km s}^{-1}$, as the left panel is a log plot. All luminosities are corrected to our adopted cosmology (Section 1).

outflows not only have $\sigma_{[\text{O III}],\text{broad}} = 700\text{--}2200 \text{ km s}^{-1}$ (median 1100 km s^{-1}), but also $\sigma_{[\text{O III}],\text{total}} = 600\text{--}2000 \text{ km s}^{-1}$ (median 1100 km s^{-1}), and line shifts of $\Delta v_{[\text{O III}],\text{broad}} = -2000\text{--}100 \text{ km s}^{-1}$ (median -1100 km s^{-1}). These are much larger than the observed limits, $\sigma_{[\text{O III}]} = 500\text{--}600$ and $\Delta v_{[\text{O III}]} = -(500\text{--}600) \text{ km s}^{-1}$, irrespective of whether we use the broad or total [O III] profile from $L_{[\text{O III}]} < 10^{43} \text{ erg s}^{-1}$ AGNs in Figure 6 or from the literature (e.g., Woo et al. 2016; Rakshit & Woo 2018).

In Figure 6, we further compare [O III] outflow kinematics at high luminosity among heavily obscured (U12; B15; Z16) type 2 quasars (V11; Harrison et al. 2014; Harrison et al. 2016; hereafter H14; H16) and unobscured quasars (H16; Shen 2016; hereafter S16; Jun et al. 2017; hereafter J17; Vietri et al. 2018 including the data from Bischetti et al. 2017; hereafter V18). It is noticeable that Hot DOGs, together with reddened quasars from Z16, show comparable or even stronger [O III] broadening or blueshift than type 1 quasars at the highest luminosity. If a simple, smooth, and toroidal geometry of the obscuring structure aligned with the broad-line region were to explain most of the obscuration (e.g., Antonucci 1993; Urry & Padovani 1995), we would expect Hot DOGs, with their high levels of reddening, to appear as type 2 AGNs seen very close to edge-on with a high line-of-sight column density. Indeed, most of the measured Seyfert types are close to type 2 ($\gtrsim 1.8$; Table 6), favoring an edge-on orientation of the AGN structure if the obscuration is well explained by geometry. Assuming the biconical outflows are aligned perpendicular to the dusty torus (e.g., Fischer et al. 2014; Marin 2016), the edge-on geometry implies a low line-of-sight velocity of the outflowing material, minimizing the observed Doppler shift and broadening of the (blueshifted/redshifted) cone and thus the total [O III] profile (e.g., Bae & Woo 2016). The observed [O III] kinematics in Figure 6 do not follow this expectation, however, but are more consistent with intrinsically higher extinction, expected to produce large blueshifts (e.g., Bae & Woo 2016). Thus, we require a different source of obscuration beyond the simple torus (e.g., Hönig et al. 2013; Asmus et al. 2016 for polar dust geometry and, e.g., Buchner & Bauer 2017 for extended obscuration within the host galaxy) or a complex velocity structure within the outflowing [O III] region (e.g., outflows with a

large bicone opening angle or the spherical outflows seen in [C II] observations of the Hot DOG W2246–0526 from Díaz-Santos et al. 2016). Although there is a large scatter in the data, we find that the outflow kinematics in Figure 6 show stronger broadening and blueshift as a function of luminosity or reddening, whereas the differences between type 1 and 2 AGN at a given luminosity are relatively minor. This suggests that the obscured quasar phase is related to the production of strong ionized gas outflows, irrespective of possible inclination effects.

Using the outflow kinematics of the broad [O III] profile under the assumption of a uniform, filled spherical/biconical outflow geometry (e.g., Maiolino et al. 2012), we estimate the outflow quantities for Hot DOGs—mass outflow rate (\dot{M}_{out}), energy injection rate (\dot{E}_{out}), and momentum flux (\dot{P}_{out})—as follows:

$$\begin{aligned}\dot{M}_{\text{out}} &= \frac{3M_{\text{gas}}v_{\text{out}}}{R_{\text{out}}} \\ \dot{E}_{\text{out}} &= \frac{1}{2}\dot{M}_{\text{out}}v_{\text{out}}^2 = \frac{3M_{\text{gas}}v_{\text{out}}^3}{2R_{\text{out}}}, \\ \dot{P}_{\text{out}} &= \dot{M}_{\text{out}}v_{\text{out}} = \frac{3M_{\text{gas}}v_{\text{out}}^2}{R_{\text{out}}}\end{aligned}\quad (1)$$

Ionized gas mass (M_{gas}), outflow size (R_{out}), and extinction-/projection-corrected outflow velocity (v_{out}) are derived as follows:

$$\begin{aligned}M_{\text{gas}} &= 4.0 \times 10^7 M_{\odot} \\ &\times \left(\frac{C}{10^{[\text{O}/\text{H}]}} \right) \left(\frac{L_{[\text{O III}],\text{broad}}}{10^{44} \text{ erg s}^{-1}} \right) \left(\frac{\langle n_e \rangle}{10^3 \text{ cm}^{-3}} \right)^{-1} \\ R_{\text{out}} &= R_{\text{out}}(L_{[\text{O III}]} > 10^{43} \text{ erg s}^{-1}) = 3 \text{ kpc} \\ v_{\text{out}} &= 2\sigma_0 = 2\sqrt{\sigma_{[\text{O III}],\text{broad}}^2 + v_{[\text{O III}],\text{broad}}^2},\end{aligned}\quad (2)$$

where $C = \langle n_e \rangle^2 / \langle n_e^2 \rangle$, n_e is the electron density, and [O/H] is the metallicity of the gas in solar units.

For Equation (2), we adopt the M_{gas} equations from Nesvadba et al. (2011) and Carniani et al. (2015) and assume $C/10^{[\text{O}/\text{H}]} = 1$, where the equations from both works become

Table 9
Outflow Quantities

Name	$\log M_{\text{gas}}$ (M_{\odot})	v_{out} (km s^{-1})	\dot{M}_{out} ($M_{\odot} \text{ yr}^{-1}$)	$\log \dot{E}_{\text{out}}$ (erg s^{-1})	$\log \dot{P}_{\text{out}}$ (dyn)	$\dot{M}_{\text{out}}/\dot{M}_{\text{acc}}$	$\dot{E}_{\text{out}}/L_{\text{bol}}$ (%)	$\dot{P}_{\text{out}} c/L_{\text{bol}}$
W0114+0812	8.12 ± 0.12	2967 ± 331	404 ± 119	45.05 ± 0.19	36.88 ± 0.15	1.82 ± 0.55	0.09 ± 0.04	0.18 ± 0.07
W0226+0514	7.53 ± 0.13	1816 ± 482	63 ± 25	43.81 ± 0.37	35.86 ± 0.26	3.37 ± 1.76	0.06 ± 0.06	0.20 ± 0.14
W1103+1826	8.28 ± 0.09	5008 ± 556	968 ± 231	45.88 ± 0.17	37.48 ± 0.13	9.61 ± 2.65	1.34 ± 0.56	1.61 ± 0.54
W1136+4236	8.61 ± 0.03	3169 ± 98	1306 ± 105	45.62 ± 0.05	37.42 ± 0.04	5.71 ± 0.51	0.32 ± 0.04	0.60 ± 0.06
W1719+0446	8.06 ± 0.45	4283 ± 225	507 ± 521	45.47 ± 0.45	37.14 ± 0.45	6.44 ± 6.78	0.66 ± 0.70	0.92 ± 0.97
W2026+0716	9.02 ± 0.04	4502 ± 149	4864 ± 465	46.49 ± 0.06	38.14 ± 0.05	7.65 ± 0.80	0.86 ± 0.12	1.15 ± 0.14
W2136+1631	8.74 ± 0.01	2051 ± 32	1143 ± 39	45.18 ± 0.02	37.17 ± 0.02	2.48 ± 0.09	0.06 ± 0.00	0.17 ± 0.01
W2216+0723	8.47 ± 0.10	3223 ± 322	971 ± 242	45.50 ± 0.16	37.29 ± 0.13	4.41 ± 1.33	0.26 ± 0.11	0.47 ± 0.17

Note. Outflow quantities are shown for [O III] lines with $S/N \geq 5$ having a broad component ($\sigma_{[\text{O III}],\text{broad}} > 400 \text{ km s}^{-1}$). Here M_{gas} is the ionized outflowing gas mass estimated using the broad [O III] profile without extinction correction on $L_{[\text{O III}],\text{broad}}$, v_{out} is the outflow velocity with extinction-/projection-correction, \dot{M}_{out} is the mass outflow rate, \dot{E}_{out} is the energy injection rate, \dot{P}_{out} is the momentum flux, \dot{M}_{acc} is the mass accretion rate (calculated as $L_{\text{bol}}/\eta c^2$ with radiative efficiency $\eta = 0.1$), and L_{bol} is the bolometric luminosity using an [O III]-to-bolometric correction factor of 3500 (Heckman et al. 2004).

identical. As for R_{out} , the $R_{\text{NLR}}-L_{[\text{O III}]}$ relation saturates at around 10 kpc beyond $L_{[\text{O III}]} \gtrsim 10^{43} \text{ erg s}^{-1}$, as noted in Section 4.3, but the radius where the outflows are effective can be smaller than the maximal extent of the outflowing [O III] line-emitting region. Observations of luminous quasars at $L_{[\text{O III}]} \gtrsim 10^{43} \text{ erg s}^{-1}$ range between ~ 1 and 10 kpc and differ upon using the spatial offset (~ 1 kpc; e.g., Carniani et al. 2015) or the spatial extent (~ 1 kpc when flux weighted, e.g., Kang & Woo 2018; ~ 5 –10 kpc when measured kinematically or above an S/N threshold, e.g., Cano-Díaz et al. 2012; Cresci et al. 2015; Perna et al. 2015; Kang & Woo 2018) of the broad/blueshifted [O III] component. We use a representative value, 3 kpc, considering the diversity in the measurement methods, and we are unable to spatially resolve the outflow size with our observations. For the objects on which both of the [S II] doublet lines are detected with $S/N \geq 3$, namely W1136+4236 and W2136+1631, we measure [S II] $\lambda 6716$ /[S II] $\lambda 6731$ ratios of 0.82 ± 0.19 and 1.02 ± 0.21 , respectively. Assuming a 10,000 K temperature, the line ratios correspond to electron densities $n_e \sim 1100$ and $\sim 600 \text{ cm}^{-3}$, respectively (Osterbrock 1989). These values are on the higher end but within the range of measurements for various AGNs (100 – 1000 cm^{-3} ; e.g., Holt et al. 2006; Nesvadba et al. 2006; Perna et al. 2015; Karouzos et al. 2016; Rakshit et al. 2017; but see also Baron & Netzer 2019). We fix $\langle n_e \rangle = 300 \text{ cm}^{-3}$ in between the boundary of the reported values due to the limited number of our measurements, but this may underestimate the outflow quantities by a factor of 2–4 if the Hot DOGs turn out to have $n_e \sim 600$ – 1000 cm^{-3} . Lastly, v_{out} is adopted from Bae & Woo (2016) and Bae et al. (2017) as a combination of the velocity dispersion and the offset to correct for dust extinction and projection effects.

There are several systematic uncertainties in using Equations (1) and (2) to derive [O III] outflow quantities (e.g., Harrison et al. 2018). First, we assume the narrow [O III] comes from a nonoutflowing region and use only the broad [O III] to measure outflow quantities. This assumption appears valid for our sample, as most of the narrow Gaussian components have offsets within $\sim 100 \text{ km s}^{-1}$ to the systemic redshift (with exceptions for W1103+1826 and W2026+0716) for non-H II BPT sources with line $S/N \geq 5$ (Table 3 and Figure 5). There are counterexamples of narrow emission lines altogether drifting against the stellar absorption line-based redshift for local AGNs (e.g., Bae & Woo 2016), but the occurrence is rare, supporting the fact that the narrow

component of the [O III] is less likely to be outflowing. Still, there are 3/9 BPT non-H II sources with [O III] $S/N \geq 5$ and narrow component widths $\sigma_{[\text{O III}],\text{narrow}} > 400 \text{ km s}^{-1}$. This is partly due to our narrow-line FWHM limit allowing up to 1200 km s^{-1} , which is an arbitrary division between a broad and a narrow line (Section 3), and we check how much the outflow quantities change if we substitute the broad [O III] component properties in Equation (2) into those of the total. We find that M_{gas} changes by a factor of 1.30–1.61 and v_{out} changes by a factor of 0.81–0.89. Here \dot{M}_{out} , \dot{E}_{out} , and \dot{P}_{out} change by factors of 1.16–1.30, 0.84–0.92, and 1.02–1.05, respectively. The overall changes are relatively insensitive to the choice of the broad or total [O III] profile, as the change in M_{gas} cancels out with that of v_{out} .

Second, we are using measured, i.e., extinction-uncorrected, [O III] luminosities to derive the outflow quantities. Though we take this effect into consideration for the outflow velocity in Equation (2), the stratified distribution of obscuring material between the lines of sight through the AGN center and the narrow-line region (Tables 1 and 8) complicates the extinction correction. As the narrow-line region is more extended than the region responsible for the majority of the dust obscuration (see Section 4.3), we adopt the Balmer decrement-based $E(B-V)$ values to estimate the extinction correction for $L_{[\text{O III}],\text{broad}}$, assuming a similar size of the outflowing [O III] line region as the narrow Balmer line region. Hot DOGs typically show $E(B-V) \sim 0.3$ – 0.7 mag (Table 8), corresponding to the [O III] extinctions by factors of ~ 3 – 9 for the Milky Way extinction curve. This reduces the M_{gas} by the same amount. As the objects with Balmer decrement values are limited, we use $L_{[\text{O III}],\text{broad}}$ observed values when deriving M_{gas} and the outflow quantities dependent on M_{gas} but interpret the values considering that they are likely underestimated. The outflow quantities normalized by the same extinction-uncorrected luminosity, or the outflow efficiencies, are more reliable under the effect of extinction.

Third, we saw an order-of-magnitude range in the measurement of both the outflow size and the electron density due to the distribution of measurements and dependence on the measurement method. Assuming our Hot DOGs span the full range of distribution in R_{out} and $\langle n_e \rangle$ at our probed luminosities, the uncertainty in the average value of R_{out} and $\langle n_e \rangle$ dividing the range by the square root of the number of objects, i.e., $10/\sqrt{8}$, will be a few times. We thus estimate the uncertainty in the

average outflow quantity (proportional to $1/R_{\text{out}} \langle n_e \rangle$) to be an order of magnitude.

We list the estimated outflow quantities for the eight Hot DOGs with $[\text{O III}] \text{ S/N} \geq 5$ and $\sigma_{[\text{O III}], \text{broad}} > 400 \text{ km s}^{-1}$ in Table 9. Extinction-uncorrected mass outflow rates are $60\text{--}4860 M_{\odot} \text{ yr}^{-1}$ (median $970 M_{\odot} \text{ yr}^{-1}$). The estimated star formation rates (SFRs) for a sample of Hot DOGs based on SED fitting are $\lesssim 300\text{--}600 M_{\odot} \text{ yr}^{-1}$ (e.g., Eisenhardt et al. 2012; Jones et al. 2014; Díaz-Santos et al. 2018), comparable to the starbursts in SMGs at similar redshifts, which show values between 100 and $1000 M_{\odot} \text{ yr}^{-1}$ (e.g., Magnelli et al. 2012). This implies that Hot DOGs have comparably higher mass outflow rates than SFRs, even when uncorrected for extinction.

We also obtain the mass-loading factor between the mass outflow and accretion, i.e., $\dot{M}_{\text{out}}/\dot{M}_{\text{acc}}$, with a mass accretion rate $\dot{M}_{\text{acc}} = L_{\text{bol}}/\eta c^2$ and radiative efficiency $\eta = 0.1$ (e.g., Soltan 1982). Using the $[\text{O III}]$ -to-bolometric correction factor (Heckman et al. 2004) removes the extinction dependence on $L_{[\text{O III}]}$ in \dot{M}_{out} when dividing by L_{bol} . The $\dot{M}_{\text{out}}/\dot{M}_{\text{acc}}$ values are 1.8–9.6 (median 5.7) so that the amount of gas outflowing is larger than that accreted, assuming Heckman et al. (2004) values are appropriate for Hot DOGs.¹⁷ Combined, we find the mass outflow rate of Hot DOGs, with an uncertainty of an order of magnitude or more on the average value, to be marginally greater than the gas consumption due to star formation or fueling the AGN itself, demonstrating the role of ionized gas outflows in depleting the ISM around the AGN and competing against gas cooling to form additional stars.

Energy injection rates range from $\dot{E}_{\text{out}} = 6.5 \times 10^{43}$ to $3.1 \times 10^{46} \text{ erg s}^{-1}$ (median $3.2 \times 10^{45} \text{ erg s}^{-1}$) without extinction correction, also being 0.058%–1.3% (median 0.32%) of L_{bol} , independent of the extinction effect. The fraction of the bolometric luminosity transferred to kinetic energy, or the feedback efficiency, is consistent with observations of luminous, obscured quasars (e.g., Z16); theoretical models and simulations of $\sim 10^3 \text{ km s}^{-1}$ winds, including kinetic energy (e.g., King 2003; Choi et al. 2012; Roth et al. 2012); or a weak outflow-induced cloud expansion (Hopkins & Elvis 2010). Also, the bolometric luminosity and the fraction of it injected into the ISM are near the limit where it can blow out the gas (e.g., see discussion in Díaz-Santos et al. 2016). Our feedback efficiencies are one to two orders of magnitude smaller than the thermal efficiencies required to match the normalization of the local BH mass–stellar velocity dispersion ($M_{\text{BH}}\text{--}\sigma_*$) relation (5%; Di Matteo et al. 2005) or those used in prescriptions for hydrodynamic cosmological simulations ($>10\%$; e.g., Dubois et al. 2014; Schaye et al. 2015; Weinberger et al. 2017), but these works have a thermal feedback mode alone or involve subgrid prescriptions in the simulations due to limited resolution. Momentum flux values are in the range $\dot{P}_{\text{out}} = 7.2 \times 10^{35}\text{--}1.4 \times 10^{38} \text{ dyn}$ (median $2.0 \times 10^{37} \text{ dyn}$), being 0.17–1.6 (median 0.60) times L_{bol}/c . Outflows are classified as energy-driven if they retain their thermal energy and momentum-driven if they radiate away. Following Tombesi et al. (2015) and Feruglio et al. (2015) for energy-conserving outflows observed in local ULIRGs (IRAS F11119+3257 and Mrk 231), the sub- L_{bol}/c momentum flux

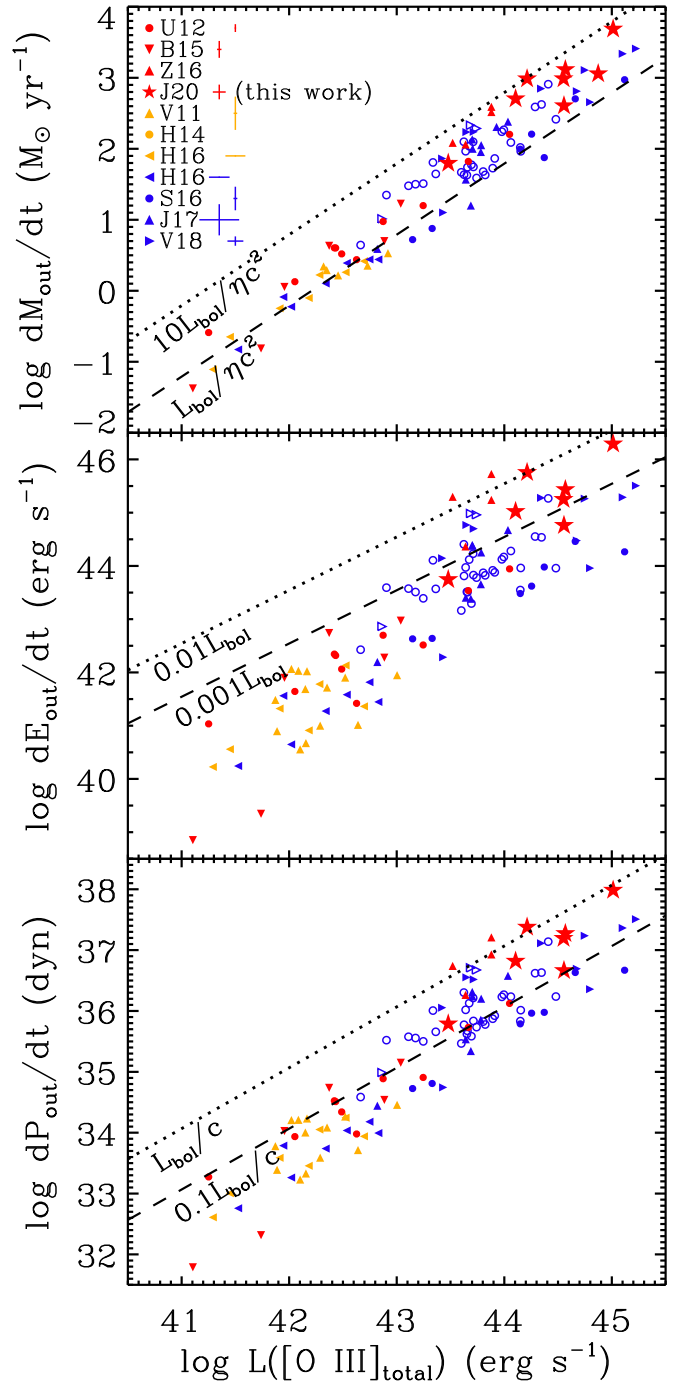


Figure 7. Estimated mass outflow rates (\dot{M}_{out}), energy injection rates (\dot{E}_{out}), and momentum fluxes (\dot{P}_{out}) against observed (extinction-uncorrected) total $[\text{O III}]$ luminosity. The colors and symbols follow those of Figure 6, and we show the outflow quantities in constant units of $L_{\text{bol}}/\eta c^2$, L_{bol} , and L_{bol}/c , respectively (dotted and dashed lines). Radiative efficiencies of $\eta = 0.1$ and an $[\text{O III}]$ -to-bolometric correction factor of 3500 (Heckman et al. 2004) are adopted. When estimating the outflow quantities, we use $\log R_{\text{out}}(\text{kpc}) = 0.41 \log L_{[\text{O III}]}(\text{erg s}^{-1}) - 14.00$ from Bae et al. (2017) for $\log L_{[\text{O III}]} < 42.63 \text{ erg s}^{-1}$ and a fixed $R_{\text{out}} = 3 \text{ kpc}$ for $\log L_{[\text{O III}]} \geq 42.63 \text{ erg s}^{-1}$. This is to match the R_{out} values adopted for Hot DOGs from Equation (2), where $R_{\text{out}}(L_{[\text{O III}]})$ using Bae et al. (2017) would exceed 3 kpc.

values for Hot DOGs are comparable to or lower than those for ULIRGs at $v_{\text{out}} \sim 10^3 \text{ km s}^{-1}$, indicating that the ionized outflows in Hot DOGs are marginally more likely to be momentum-driven than energy-driven. We summarize our findings in Figure 7. Hot DOGs show among the strongest

¹⁷ The Heckman et al. (2004) bolometric correction may not directly apply for Hot DOGs if they are a different population than typical AGNs. The median and scatter of L_{bol} ratios using bolometric corrections from $L_{[\text{O III}]}$ and L_{5100} for eight Hot DOGs with a non-H II BPT classification are $0.08 \pm 0.87 \text{ dex}$.

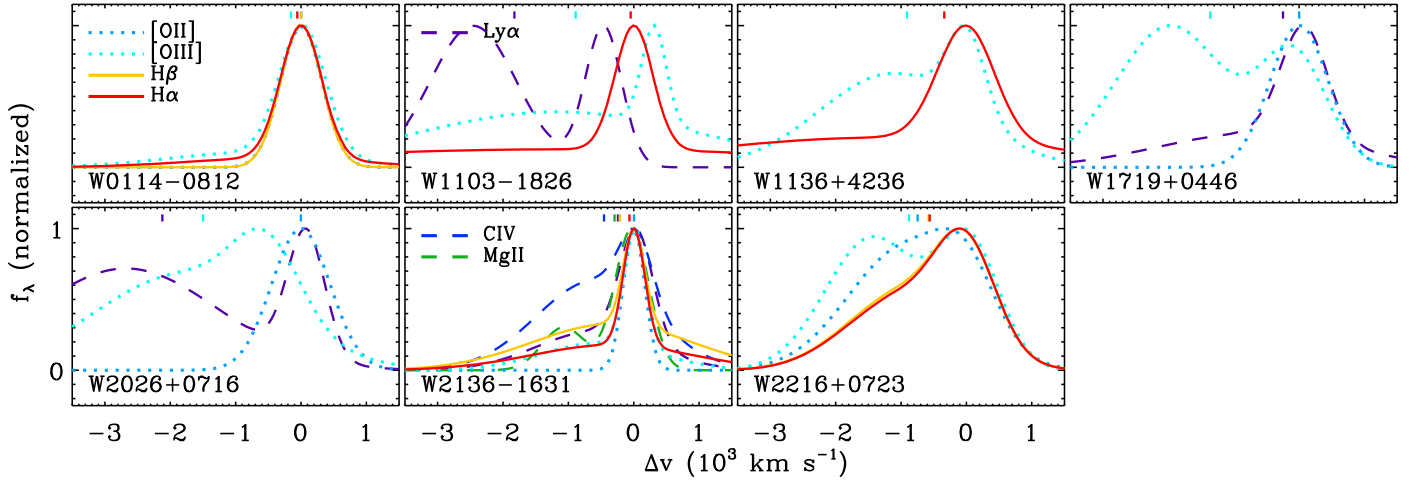


Figure 8. Model profiles to the emission lines with $S/N \geq 5$ that have either a significantly broad ($\sigma_{\text{broad/narrow}} > 400 \text{ km s}^{-1}$) Balmer line (W0114–0812, W1103–1826, W1136+4236, W2136–1631, and W2216+0723) or an [O II] line (W1719+0446, W2026+0716, and W2216+0723). The colors for the lines follow those of Figure 2, and the rest-frame UV lines (Ly α , purple; C IV, blue; Mg II, green) are shown dashed, oxygen lines ([O II] $\lambda 3727$, light blue; [O III] $\lambda 5007$, cyan) are dotted, and Balmer lines (H β , yellow; H α , red) are solid. The first moment of the total profile is shown on top of the models with corresponding colors.

outflow quantities (\dot{M}_{out} , \dot{E}_{out} , \dot{P}_{out}) and outflow efficiencies ($\dot{M}_{\text{out}}/\dot{M}_{\text{acc}}$, $\dot{E}_{\text{out}}/L_{\text{bol}}$, $\dot{P}_{\text{out}}c/L_{\text{bol}}$) compared to the AGN samples in the literature.

4.5. Interpretation of Broad Lines in Obscured AGNs

Having seen the occurrence and strength of [O III] outflows in our luminous, obscured AGN sample, we now assess the usefulness of broad emission lines in measuring M_{BH} for highly obscured AGNs. We overplot in Figure 8 the normalized profiles of prominent lines for the sources with potential outflows in addition to the [O III] line. The figure includes the 5/7 BPT non-H II Hot DOGs with significantly broad H α ($\sigma_{\text{H}\alpha, \text{broad/narrow}} > 400 \text{ km s}^{-1}$) with $S/N > 5$ from Table 3 (W0114–0812, W1103–1826, W1136+4236, W2136–1631, and W2216+0723). The normalized broad Balmer line components are weaker than the broad [O III] but are blueshifted for all five objects, with absolute values comparable to or smaller than the broad [O III] blueshift with a fraction of 0.53–1.23 times (median 0.65). This trend is also seen in the first moment of the Balmer lines (Δv in Table 3) being blueshifted, but not as much as that of the [O III].

The broadening of the Balmer line might come from the broad-line region, with blueshifts indicating outflows within the broad-line region (e.g., Vietri et al. 2018) or the broad-line region simply being highly obscured. We check this by calculating the Balmer decrement of objects having $S/N \geq 5$ in H α and showing a broad component in both H α /H β (W1103–1826, W1136+4236, W2136–1631, and W2216+0723). The values are 1.93 ± 1.02 , 4.28 ± 0.87 , 1.93 ± 0.22 , and 5.95 ± 2.17 , respectively, all comparable to or smaller than the narrow Balmer decrements in Table 8. This is inconsistent with the expected higher extinction (and thereby higher Balmer decrements) toward the broad-line region compared to the narrow-line region, assuming that the intrinsic Balmer decrements of the broad-line region for Hot DOGs are comparable to the observed values for luminous type 1 quasars at $z \sim 2$ (median and scatter of 3.2 ± 1.4 ; Shen & Liu 2012), which themselves are comparable to the intrinsic values for the narrow lines (3.1; e.g., Osterbrock 1989). Therefore, we find it more likely that broad and blueshifted Balmer lines

Table 10
Accretion Rates

Name	$\log M_{\text{BH}}$ (M_{\odot})	f_{Edd}	$f_{\text{Edd}}(M_{\text{BH}} < 10^{10} M_{\odot})$
W0114–0812	9.34 ± 0.15	2.19 ± 0.77	>0.48
W0147–0923	9.20 ± 0.35	9.02 ± 7.25	>1.44
W0226+0514	8.95 ± 0.28	8.08 ± 5.24	>0.71
W1103–1826	9.18 ± 0.30	3.60 ± 2.49	>0.54
W1136+4236	$<9.96 \pm 0.13$	$>0.28 \pm 0.09$	>0.26
W1719+0446	$<10.01 \pm 0.46$	$>0.81 \pm 0.86$	>0.83
W2026+0716	$<10.01 \pm 0.27$	$>0.43 \pm 0.27$	>0.45
W2136–1631	8.08 ± 0.07	15.98 ± 2.40	>0.19
W2216+0723	$<10.02 \pm 0.17$	$>0.23 \pm 0.09$	>0.24

Note. Here M_{BH} is the mass assuming the local $M_{\text{BH}}-\sigma_*$ relation and using σ_{narrow} as a substitute for σ_* from [O II], H β , or H α lines with $S/N \geq 5$. Here f_{Edd} is the Eddington ratio, $L_{\text{bol}}/L_{\text{Edd}}$, where L_{bol} is derived from the SED fit (e.g., Figure 1), and L_{Edd} is the Eddington luminosity. The f_{Edd} values are derived using $\log M_{\text{BH}}/M_{\odot} = 8.49 + 4.377 \log \{\sigma_*/(\text{km s}^{-1})/200\}$ (Kormendy & Ho 2013) and a 1–1 relation between σ_* and σ_{narrow} ; e.g., Bennert et al. 2018) and an observed upper limit of $M_{\text{BH}} \sim 10^{10} M_{\odot}$ for the most massive SDSS quasars (Jun et al. 2017).

originate outside the broad-line region and that they are due to outflows within the narrow-line region. This is also consistent with the objects not showing a broad H α (2/7) still having $\sigma_{\text{H}\alpha, \text{broad/narrow}} > 300 \text{ km s}^{-1}$, which is on the broader side to be explained by nonoutflowing motion unless the host galaxies of Hot DOGs have grown to sufficiently massive bulges at $z \sim 2$.

Following Wu et al. (2018), we check if the Balmer line outflows are as strong as the [O III] outflows by fitting the rest-frame 3500–7000 Å spectra with a common broad-line center and width and calculating the F -distribution probability of the reduced χ^2 from the fit having a statistically significant improvement. Out of the $S/N \geq 5$ spectra, 1/9 (W0147–0923) has an improvement (95% or higher F -distribution probability) such that the broad Balmer lines are indistinguishable from the outflowing [O III] component, but 7/9 (including all of the broad H α sources in Figure 8) yield significantly improved fits when the broad [O III] center and width are detached from the rest of the lines. We thus can rule out the case where all of

the broad Balmer lines are showing outflows as strong as the [O III], in accord with Wu et al. (2018) and consistent with weaker but similar Balmer line kinematics as the [O III] found in SDSS type 2 quasars (e.g., Kang et al. 2017).

In addition to the likelihood of outflows in the narrow Balmer line region for some Hot DOGs, we plot in the remaining panels of Figure 8 the 3/6 BPT non-H II sources with significantly broad [O II] ($\sigma_{[\text{O II}],\text{broad/narrow}} > 400 \text{ km s}^{-1}$; W1719+0446, W2026+0716, W2216+0723) with S/N > 5. Additionally, 1/3 of the remaining (3/6) sources (W0114-0812) shows $\sigma_{[\text{O II}],\text{broad/narrow}} > 300 \text{ km s}^{-1}$. This can be explained by either strong AGN outflows broadening the [O II] line profile or the kinematics of the ISM in the star-forming region being highly disturbed by AGN outflows and/or galaxy merging (e.g., Díaz-Santos et al. 2016, 2018). As [O II] is a forbidden line, a fraction of them being broad adds support for the presence of outflows and hints at an \sim kiloparsec-scale, narrow-line region origin for at least some of the broadened Balmer lines.

The presence of outflowing material within the Balmer or even the [O II] lines can cause serious misinterpretation when using the broad emission line width to measure M_{BH} . Although we are limited to a single object (W2136-1631) in Figure 8 covering all of the major UV/optical broad emission lines, the hydrogen lines (Ly α , H β , H α) and Mg II profiles are indistinguishable from [O III], with C IV showing a stronger broad/blueshifted wing component. This suggests that not only the Balmer lines but also the rest-frame UV broad emission lines could be contaminated by outflows within the narrow-line region. Therefore, not only the M_{BH} measurements reported for Hot DOGs (e.g., Ricci et al. 2017a; Tsai et al. 2018; Wu et al. 2018) but also any M_{BH} measurement for a highly obscured AGN with a broad and blueshifted permitted emission line should be carefully tested for the presence of outflows through signatures of broad and blueshifted forbidden lines (e.g., Alexander et al. 2008; Ricci et al. 2017c), especially at $L_{[\text{O III}]} > 10^{42} \text{ erg s}^{-1}$ (Figure 6). On the other hand, we expect that the M_{BH} values for Hot DOGs from emission lines likely coming from scattered light (e.g., Assef et al. 2016, 2019) are unlikely to be affected by outflows.

4.6. Eddington Ratio for Hot DOGs

We alternatively estimate M_{BH} and the Eddington ratios (f_{Edd}) shown in Table 10 using the $M_{\text{BH}}-\sigma_*$ relation and the width of the common narrow component of [O II]/Balmer lines, noting that σ_* is similar to narrow emission line widths but with a large uncertainty (a factor of ~ 2 ; e.g., Greene & Ho 2005a; Zakamska & Greene 2014; Bennert et al. 2018). Here we select the narrow-line width from [O II]/Balmer lines instead of [O III] to minimize blending from outflows. Considering the dispersion of the $M_{\text{BH}}-\sigma_*$ relation itself (a factor of 2–3; e.g., Kormendy & Ho 2013; Woo et al. 2013) and the possibility of a systematic offset for various types of AGNs compared to the local inactive galaxies on the BH–galaxy scaling relation (up to a factor of several; e.g., Kim et al. 2008; U12; Sexton et al. 2019), the M_{BH} estimates for Hot DOGs could be inaccurate by up to an order of magnitude. Having in mind those uncertainties, we find most of the M_{BH} values to be on the order of $10^9 M_\odot$, while those associated with $\sigma_{\text{narrow}} > 400 \text{ km s}^{-1}$ are given with upper limits and show values around $\sim 10^{10} M_\odot$. We convert the M_{BH} estimates and use the L_{bol} from the extinction-corrected 5100 Å luminosity with a bolometric correction (e.g., Figure 1) into

the Eddington ratio $f_{\text{Edd}} = L_{\text{bol}}/L_{\text{Edd}}$, which ranges on the order of unity to 10. This can be interpreted as the AGN accretion being highly effective near or even beyond its Eddington limit, but there are possibilities of a systematic offset in f_{Edd} for Hot DOGs.

To better tell whether the super-Eddington accretion seen in some of the Hot DOGs is real or due to systematic overestimation, we estimate the f_{Edd} values again from considering an upper limit of $M_{\text{BH}} \sim 10^{10} M_\odot$ for the most massive $z \sim 2$ quasars (Jun et al. 2017). Listed in Table 10, the corresponding lower limits on f_{Edd} values are around 0.2–1.4 (mean 0.6), indicating near-Eddington-limited accretion even if M_{BH} reaches $\sim 10^{10} M_\odot$ and super-Eddington accretion if $M_{\text{BH}} \lesssim 5 \times 10^9 M_\odot$. In any case, we find without any measurement of M_{BH} that Hot DOGs are likely accreting near or beyond the Eddington limit. If we trust the f_{Edd} values from the $M_{\text{BH}}-\sigma_*$ relation, however, 4/9 sources have f_{Edd} exceeding 3 (but with large measurement uncertainties), which is hard to explain with models allowing accretion modes up to several times the Eddington limit (e.g., see discussion in Tsai et al. 2018). We thus find it likely that some of our f_{Edd} values are largely overestimated due to either an underestimated M_{BH} or an overestimated L_{bol} .

Under the merger-driven AGN triggering mechanism (e.g., Hopkins et al. 2008; Hickox et al. 2009), starbursts in the merging system will be followed by obscured BH growth. Using a simple BH–galaxy mass scaling relation, M_{BH} values for Hot DOGs are more likely to be higher relative to the central host mass due to the time delay between BH and galaxy growth (e.g., U12) and the bulge formation lagging the BH growth (e.g., Peng et al. 2006; Jun et al. 2017) at $z \sim 2$. Alternative explanations for extremely high f_{Edd} values for Hot DOGs could be due to L_{bol} being overestimated by anisotropic radiation (e.g., Abramowicz et al. 1988; Wang et al. 2014), but this is less likely to be significant, as the SED peaking in the IR is relatively isotropic. Gravitational lensing is also a less likely explanation given the morphologies of Hot DOGs imaged by the *Hubble Space Telescope* (e.g., Tsai et al. 2015).

To summarize, our sample of Hot DOGs shows high f_{Edd} values, with lower limits often near the Eddington limit. This may be produced by underestimated M_{BH} (σ_*) values, but with large potential uncertainties in both the M_{BH} and L_{bol} , it is hard to tell from our data whether super-Eddington accretion is occurring. The efficient accretion probed by our objects is consistent with scenarios with BH feeding in luminous, obscured AGNs triggering strong ionized gas outflows. Our sample is also in line with the more X-ray-luminous population of SMGs showing a stronger, near-Eddington-limited accretion than the X-ray-weaker counterpart (Alexander et al. 2008), following the evolutionary model predictions. However, it is in tension with the absence of a hard X-ray-selected local AGN population with high f_{Edd} and $E(B-V)$ (Ricci et al. 2017c), suggesting that the local population might simply lack the rapidly accreting, obscured AGN seen at $z \sim 2$ (H. D. Jun et al. 2019, in preparation).

5. Summary

We classified the rest-frame UV–optical spectra of 12 Hot DOGs at $z \sim 2$ and quantified the ionized gas outflows in [O III]. The main results are summarized below.

1. The redshifts for Hot DOGs in this sample peak around 2–3 and are consistent with the distribution obtained from rest-frame UV spectroscopy. Using a wide spectral window in this study, we found two mismatches out of eight previous redshift estimates that were based on narrower spectral coverage.
2. On the BPT diagram, 7/8 Hot DOGs are classified as AGNs, confirming the expectation from the strong mid-IR peak in their SEDs. The Seyfert types are 1.8 or higher for 6/8 objects, indicating that the broad-line regions are mostly obscured. The [O II]/[O III] ratios, which potentially trace the relative contribution of star formation over AGN activity, vary between 0.1 and 2.6 and are lower for AGNs exclusively in all three BPT diagrams.
3. Extinction within the narrow-line region estimated from the Balmer decrement indicates $E(B-V)$ values around 0.3–0.7 mag. This is about an order of magnitude smaller than the values from SED modeling, indicating that most of the obscuration is concentrated interior to the narrow-line region. As the narrow-line region is extended up to kiloparsec scales, however, we infer that obscuration exists throughout the host galaxy. The $E(B-V)$ values from $\text{EW}_{[\text{O III}]}$ independently tracing the obscuration toward the AGN center have lower limits of 0–1.1 mag.
4. Ionized gas outflows are seen in 8/9 [O III] lines with $S/N \geq 5$, broad enough ($\sigma_{[\text{O III}],\text{broad}} > 400 \text{ km s}^{-1}$) to be distinguished from gravitational motion in the most massive bulges. The median broadening and blueshift of the broad [O III] component are 1100 and -1100 km s^{-1} , respectively, much stronger than lower-luminosity quasars from the literature. The outflow kinematics for Hot DOGs, together with other highly obscured AGNs, are contrary to the simplest orientation-driven models of type 2 AGNs. Comparing with the literature, the luminosity dependence on outflow kinematics is greater than that of AGN type, favoring a physical and evolutionary origin for producing ionized gas outflows.

Normalized median outflow quantities are $\dot{M}_{\text{out}}/\dot{M}_{\text{acc}} \sim 5.7$, $\dot{E}_{\text{out}}/L_{\text{bol}} \sim 0.32\%$, and $\dot{P}_{\text{out}}/(L_{\text{bol}}/c) \sim 0.60$, all corrected for extinction but having a large scatter and uncertainty (\sim an order of magnitude each). Mass outflow rates are comparable to or higher than SFRs or mass accretion rates, indicating that outflows in Hot DOGs may be efficient in depleting gas, whereas the energy injection rate and momentum flux are sufficient to quench the star formation in galaxy simulations.








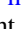

5. We find further hints of outflow signatures in $S/N \geq 5$ H α lines (5/7), showing a broad ($\sigma_{\text{broad/narrow}} > 400 \text{ km s}^{-1}$) component blueshifted by 0.5–1.2 times that of the [O III]. Even some $S/N \geq 5$ [O II] lines (3/6) have $\sigma_{\text{broad/narrow}} > 400 \text{ km s}^{-1}$, supporting the presence of ionized gas outflows in multiple ionization states. The signs for outflows in the Balmer lines and the relatively higher obscuration toward the broad-line region than the narrow-line region can complicate M_{BH} estimation for luminous, obscured AGNs.
6. Alternative estimates of the Eddington ratio based on the $M_{\text{BH}}-\sigma_{\text{narrow}}$ relation and the observed upper limit on the M_{BH} values for AGNs consistently suggest near-Eddington or even stronger accretion, supporting that luminous,

obscured AGN activity from vast amounts of gas fed into the BH is responsible for producing feedback.

We summarize several remaining issues on outflows from luminous, obscured AGNs. We note that ionized gas represents only a fraction of the total gas, and our outflow quantities are commonly underestimated. Observations of multiphase outflows from gas spatially resolved and distributed in various locations of the AGNs (e.g., Díaz-Santos et al. 2016, 2018; Fiore et al. 2017) will help us understand the dominant phase and location of the energy output injected into the ISM. As we find a high fraction and strength of ionized gas outflows among the most luminous, obscured AGNs, the demographics of the merger-triggered AGN activity along various observed samples should eventually be analyzed to resolve the issue of whether the scarcity of the most massive galaxies matches the energetics of AGN feedback quenching star formation.

We thank the anonymous referee for the valuable comments improving the paper and the ESO staff for kindly observing and providing processed data products. This research was supported by the Basic Science Research Program through the National Research Foundation of Korea (NRF) funded by the Ministry of Education (NRF-2017R1A6A3A04005158). R.J.A. was supported by FONDECYT grant No. 1191124. F.E.B. acknowledges support from CONICYT-Chile (Basal AFB-170002) and the Ministry of Economy, Development, and Tourism’s Millennium Science Initiative through grant IC120009, awarded to the Millennium Institute of Astrophysics, MAS. J.W. acknowledges support from MSTC through grant 2016YFA0400702 and NSFC 11673029. This publication makes use of data products from the *Wide-field Infrared Survey Explorer*, which is a joint project of the University of California, Los Angeles, and the Jet Propulsion Laboratory/California Institute of Technology, funded by the National Aeronautics and Space Administration.

ORCID iDs

Hyunsung D. Jun  <https://orcid.org/0000-0003-1470-5901>
 Roberto J. Assef  <https://orcid.org/0000-0002-9508-3667>
 Franz E. Bauer  <https://orcid.org/0000-0002-8686-8737>
 Andrew Blain  <https://orcid.org/0000-0001-7489-5167>
 Tanio Díaz-Santos  <https://orcid.org/0000-0003-0699-6083>
 Daniel Stern  <https://orcid.org/0000-0003-2686-9241>
 Chao-Wei Tsai  <https://orcid.org/0000-0002-9390-9672>
 Edward, L. Wright  <https://orcid.org/0000-0001-5058-1593>
 Jingwen Wu  <https://orcid.org/0000-0001-7808-3756>

References

- Abramowicz, M. A., Czerny, B., Lasota, J. P., et al. 1988, *ApJ*, **332**, 646
 Alexander, D. M., Brandt, W. N., Smail, I., et al. 2008, *AJ*, **135**, 1968
 Antonucci, R. 1993, *ARA&A*, **31**, 473
 Asmus, D., Hönig, S. F., & Gandhi, P. 2016, *ApJ*, **822**, 109
 Assef, R. J., Brightman, M., Walton, D. J., et al. 2019, arXiv:1905.04320
 Assef, R. J., Eisenhardt, P. R. M., Stern, D., et al. 2015, *ApJ*, **804**, 27
 Assef, R. J., Walton, D. J., Brightman, M., et al. 2016, *ApJ*, **819**, 111
 Bae, H.-J., & Woo, J.-H. 2014, *ApJ*, **795**, 30
 Bae, H.-J., & Woo, J.-H. 2016, *ApJ*, **828**, 97
 Bae, H.-J., Woo, J.-H., Karouzos, M., et al. 2017, *ApJ*, **837**, 91
 Baldwin, J. A. 1977, *ApJ*, **214**, 679
 Baldwin, J. A., Phillips, M. M., & Terlevich, R. 1981, *PASP*, **93**, 5
 Banerji, M., Alaghband-Zadeh, S., Hewett, P. C., & McMahon, R. G. 2015, *MNRAS*, **447**, 3368
 Banerji, M., McMahon, R. G., Hewett, P. C., et al. 2012, *MNRAS*, **427**, 2275

- Banerji, M., McMahon, R. G., Hewett, P. C., Gonzalez-Solares, E., & Kposov, S. E. 2013, *MNRAS*, **429**, L55
- Baron, D., & Netzer, H. 2019, *MNRAS*, **486**, 4290
- Bennert, V. N., Loveland, D., Donohue, E., et al. 2018, *MNRAS*, **481**, 138
- Bischetti, M., Piconcelli, E., Vietri, G., et al. 2017, *A&A*, **598**, A122
- Blain, A. W., Smail, I., Ivison, R. J., et al. 2002, *PhR*, **369**, 111
- Bridge, C. R., Blain, A., Borys, C. J. K., et al. 2013, *ApJ*, **769**, 91
- Brotherton, M. S. 1996, *ApJS*, **102**, 1
- Brusa, M., Bongiorno, A., Cresci, G., et al. 2015, *MNRAS*, **446**, 2394
- Buchner, J., & Bauer, F. E. 2017, *MNRAS*, **465**, 4348
- Cano-Díaz, M., Maiolino, R., Marconi, A., et al. 2012, *A&A*, **537**, L8
- Carniani, S., Marconi, A., Maiolino, R., et al. 2015, *A&A*, **580**, A102
- Chapman, S. C., Blain, A. W., Smail, I., & Ivison, R. J. 2005, *ApJ*, **622**, 772
- Choi, E., Ostriker, J. P., Naab, T., & Johansson, P. H. 2012, *ApJ*, **754**, 125
- Crenshaw, D. M., & Kraemer, S. B. 2000, *ApJL*, **532**, L101
- Crenshaw, D. M., Schmitt, H. R., Kraemer, S. B., Mushotzky, R. F., & Dunn, J. P. 2010, *ApJ*, **708**, 419
- Cresci, G., Mainieri, V., Brusa, M., et al. 2015, *ApJ*, **799**, 82
- Croton, D. J., Springel, V., White, S. D. M., et al. 2006, *MNRAS*, **365**, 11
- Dey, A., Soifer, B. T., Desai, V., et al. 2008, *ApJ*, **677**, 943
- Di Matteo, T., Springel, V., & Hernquist, L. 2005, *Natur*, **433**, 604
- Díaz-Santos, T., Assef, R. J., Blain, A. W., et al. 2016, *ApJL*, **816**, L6
- Díaz-Santos, T., Assef, R. J., Blain, A. W., et al. 2018, *Sci*, **362**, 1034
- Dimitrijević, M. S., Popović, L. Č., Kovačević, J., Dačić, M., & Ilić, D. 2007, *MNRAS*, **374**, 1181
- DiPompeo, M. A., Hickox, R. C., Carroll, C. M., et al. 2018, *ApJ*, **856**, 76
- Dubois, Y., Pichon, C., Welker, C., et al. 2014, *MNRAS*, **444**, 1453
- Eisenhardt, P. R. M., Wu, J., Tsai, C.-W., et al. 2012, *ApJ*, **755**, 173
- Fabian, A. C. 2012, *ARA&A*, **50**, 455
- Fan, L., Han, Y., Fang, G., et al. 2016, *ApJL*, **822**, L32
- Farrah, D., Petty, S., Connolly, B., et al. 2017, *ApJ*, **844**, 106
- Ferland, G. J., & Osterbrock, D. E. 1986, *ApJ*, **300**, 658
- Feruglio, C., Fiore, F., Carniani, S., et al. 2015, *A&A*, **583**, A99
- Fiore, F., Feruglio, C., Shankar, F., et al. 2017, *A&A*, **601**, A143
- Fischer, T. C., Crenshaw, D. M., Kraemer, S. B., et al. 2014, *ApJ*, **785**, 25
- Freudling, W., Romaniello, M., Bramich, D. M., et al. 2013, *A&A*, **559**, A96
- Glikman, E., Lacy, M., LaMassa, S., et al. 2018, *ApJ*, **861**, 37
- Glikman, E., Urrutia, T., Lacy, M., et al. 2012, *ApJ*, **757**, 51
- Gobat, R., Daddi, E., Magdis, G., et al. 2018, *NatAs*, **2**, 239
- Greene, J. E., Alexandroff, R., Strauss, M. A., et al. 2014, *ApJ*, **788**, 91
- Greene, J. E., & Ho, L. C. 2005a, *ApJ*, **627**, 721
- Greene, J. E., & Ho, L. C. 2005b, *ApJ*, **630**, 122
- Hainline, K. N., Hickox, R. C., Greene, J. E., et al. 2014, *ApJ*, **787**, 65
- Hamann, F., Zakamska, N. L., Ross, N., et al. 2017, *MNRAS*, **464**, 3431
- Harrison, C. M., Alexander, D. M., Mullaney, J. R., et al. 2016, *MNRAS*, **456**, 1195
- Harrison, C. M., Alexander, D. M., Mullaney, J. R., & Swinbank, A. M. 2014, *MNRAS*, **441**, 3306
- Harrison, C. M., Costa, T., Tadhunter, C. N., et al. 2018, *NatAs*, **2**, 198
- Heckman, T. M., Kauffmann, G., Brinchmann, J., et al. 2004, *ApJ*, **613**, 109
- Hickox, R. C., Jones, C., Forman, W. R., et al. 2009, *ApJ*, **696**, 891
- Ho, L. C. 2005, *ApJ*, **629**, 680
- Holt, J., Tadhunter, C., Morganti, R., et al. 2006, *MNRAS*, **370**, 1633
- Hönig, S. F., & Beckert, T. 2007, *MNRAS*, **380**, 1172
- Hönig, S. F., Kishimoto, M., Tristram, K. R. W., et al. 2013, *ApJ*, **771**, 87
- Hopkins, P. F., & Elvis, M. 2010, *MNRAS*, **401**, 7
- Hopkins, P. F., Hernquist, L., Cox, T. J., & Kereš, D. 2008, *ApJS*, **175**, 356
- Husemann, B., Wisotzki, L., Sánchez, S. F., & Jahnke, K. 2013, *A&A*, **549**, A43
- Im, M., Griffiths, R. E., & Ratnatunga, K. U. 1997, *ApJ*, **475**, 457
- Jones, S. F., Blain, A. W., Stern, D., et al. 2014, *MNRAS*, **443**, 146
- Jun, H. D., & Im, M. 2013, *ApJ*, **779**, 104
- Jun, H. D., Im, M., Kim, D., & Stern, D. 2017, *ApJ*, **838**, 41
- Jun, H. D., Im, M., Lee, H. M., et al. 2015, *ApJ*, **806**, 109
- Kang, D., & Woo, J.-H. 2018, *ApJ*, **864**, 124
- Kang, D., Woo, J.-H., & Bae, H.-J. 2017, *ApJ*, **845**, 131
- Karouzos, M., Woo, J.-H., & Bae, H.-J. 2016, *ApJ*, **833**, 171
- Kauffmann, G., Heckman, T. M., Tremonti, C., et al. 2003, *MNRAS*, **346**, 1055
- Kausch, W., Noll, S., Smette, A., et al. 2015, *A&A*, **576**, A78
- Kewley, L. J., Dopita, M. A., Sutherland, R. S., Heisler, C. A., & Trevena, J. 2001, *ApJ*, **556**, 121
- Kewley, L. J., Groves, B., Kauffmann, G., & Heckman, T. 2006, *MNRAS*, **372**, 961
- Kim, D., & Im, M. 2018, *A&A*, **610**, A31
- Kim, M., Ho, L. C., & Im, M. 2006, *ApJ*, **642**, 702
- Kim, M., Ho, L. C., Peng, C. Y., et al. 2008, *ApJ*, **687**, 767
- King, A. 2003, *ApJL*, **596**, L27
- Kormendy, J., & Ho, L. C. 2013, *ARA&A*, **51**, 511
- Lacy, M., Ridgway, S. E., Sajina, A., et al. 2015, *ApJ*, **802**, 102
- Leung, G. C. K., Coil, A. L., Azadi, M., et al. 2017, *ApJ*, **849**, 48
- Liu, G., Zakamska, N. L., & Greene, J. E. 2014, *MNRAS*, **442**, 1303
- Liu, G., Zakamska, N. L., Greene, J. E., Nesvadba, N. P. H., & Liu, X. 2013, *MNRAS*, **436**, 2576
- Maddox, N. 2018, *MNRAS*, **480**, 5203
- Magnelli, B., Lutz, D., Santini, P., et al. 2012, *A&A*, **539**, A155
- Maiolino, R., Gallerani, S., Neri, R., et al. 2012, *MNRAS*, **425**, L66
- Marin, F. 2016, *MNRAS*, **460**, 3679
- Markwardt, C. B. 2009, in ASP Conf. Ser. 411, *Astronomical Data Analysis Software and Systems XVIII*, ed. D. A. Bohlender, D. Durand, & P. Dowler (San Francisco, CA: ASP), 251
- Mullaney, J. R., Alexander, D. M., Fine, S., et al. 2013, *MNRAS*, **433**, 622
- Murakami, H., Baba, H., Barthel, P., et al. 2007, *PASJ*, **59**, 369
- Narayanan, D., Dey, A., Hayward, C. C., et al. 2010, *MNRAS*, **407**, 1701
- Nenkova, M., Sirocky, M. M., Nikutta, R., Ivezić, Ž., & Elitzur, M. 2008, *ApJ*, **685**, 160
- Nesvadba, N. P. H., Lehnert, M. D., Eisenhauer, F., et al. 2006, *ApJ*, **650**, 693
- Nesvadba, N. P. H., Polletta, M., Lehnert, M. D., et al. 2011, *MNRAS*, **415**, 2359
- Neugebauer, G., Habing, H. J., van Duinen, R., et al. 1984, *ApJL*, **278**, L1
- Osterbrock, D. E. 1981, *ApJ*, **249**, 462
- Osterbrock, D. E. 1989, *Astrophysics of Gaseous Nebulae and Active Galactic Nuclei* (Mill Valley, CA: Univ. Science Books)
- Peng, C. Y., Impey, C. D., Rix, H.-W., et al. 2006, *ApJ*, **649**, 616
- Perna, M., Brusa, M., Cresci, G., et al. 2015, *A&A*, **574**, A82
- Perrotta, S., Hamann, F., Zakamska, N. L., et al. 2019, *MNRAS*, **488**, 4126
- Polletta, M., Weedman, D., Hönig, S., et al. 2008, *ApJ*, **675**, 960
- Rakshit, S., Stalín, C. S., Chand, H., & Zhang, X.-G. 2017, *ApJS*, **229**, 39
- Rakshit, S., & Woo, J.-H. 2018, *ApJ*, **865**, 5
- Ricci, C., Assef, R. J., Stern, D., et al. 2017a, *ApJ*, **835**, 105
- Ricci, C., Bauer, F. E., Treister, E., et al. 2017b, *MNRAS*, **468**, 1273
- Ricci, C., Trakhtenbrot, B., Koss, M. J., et al. 2017c, *Natur*, **549**, 488
- Richards, G. T., Lacy, M., Storrie-Lombardi, L. J., et al. 2006, *ApJS*, **166**, 470
- Rigby, J. R., Rieke, G. H., Donley, J. L., Alonso-Herrero, A., & Pérez-González, P. G. 2006, *ApJ*, **645**, 115
- Ross, N. P., Hamann, F., Zakamska, N. L., et al. 2015, *MNRAS*, **453**, 3932
- Roth, N., Kasen, D., Hopkins, P. F., & Quataert, E. 2012, *ApJ*, **759**, 36
- Sanders, D. B., & Mirabel, I. F. 1996, *ARA&A*, **34**, 749
- Sanders, D. B., Soifer, B. T., Elias, J. H., et al. 1988, *ApJ*, **325**, 74
- Schaye, J., Crain, R. A., Bower, R. G., et al. 2015, *MNRAS*, **446**, 521
- Schlafly, E. F., & Finkbeiner, D. P. 2011, *ApJ*, **737**, 103
- Sexton, R. O., Canalizo, G., Hiner, K. D., et al. 2019, *ApJ*, **878**, 101
- Shen, Y. 2016, *ApJ*, **817**, 55
- Shen, Y., & Ho, L. C. 2014, *Natur*, **513**, 210
- Shen, Y., & Liu, X. 2012, *ApJ*, **753**, 125
- Shen, Y., Richards, G. T., Strauss, M. A., et al. 2011, *ApJS*, **194**, 45
- Silk, J., & Rees, M. J. 1998, *A&A*, **331**, L1
- Smette, A., Sana, H., Noll, S., et al. 2015, *A&A*, **576**, A77
- Soltan, A. 1982, *MNRAS*, **200**, 115
- Stern, D., Lansbury, G. B., Assef, R. J., et al. 2014, *ApJ*, **794**, 102
- Storchi-Bergmann, T., Dall'Agnol, B., Longo Micchi, L. F., et al. 2018, *ApJ*, **868**, 14
- Storey, P. J., & Zeppen, C. J. 2000, *MNRAS*, **312**, 813
- Temple, M. J., Banerji, M., Hewett, P. C., et al. 2019, *MNRAS*, **487**, 2594
- Toba, Y., Bae, H.-J., Nagao, T., et al. 2017, *ApJ*, **850**, 140
- Tombesi, F., Meléndez, M., Veilleux, S., et al. 2015, *Natur*, **519**, 436
- Tsai, C.-W., Eisenhardt, P. R. M., Jun, H. D., et al. 2018, *ApJ*, **868**, 15
- Tsai, C.-W., Eisenhardt, P. R. M., Wu, J., et al. 2015, *ApJ*, **805**, 90
- Urrutia, T., Lacy, M., Spoon, H., et al. 2012, *ApJ*, **757**, 125
- Urry, C., & Padovani, P. 1995, *PASP*, **107**, 803
- Veilleux, S., Cecil, G., Bland-Hawthorn, J., et al. 1994, *ApJ*, **433**, 48
- Vernet, J., Dekker, H., D'Odorico, S., et al. 2011, *A&A*, **536**, A105
- Vietri, G., Piconcelli, E., Bischetti, M., et al. 2018, *A&A*, **617**, A81
- Villar-Martín, M., Humphrey, A., Delgado, R. G., Colina, L., & Arribas, S. 2011, *MNRAS*, **418**, 2032
- Wang, J.-M., Qiu, J., Du, P., et al. 2014, *ApJ*, **797**, 65
- Weinberger, R., Springel, V., Hernquist, L., et al. 2017, *MNRAS*, **465**, 3291

- Werner, M. W., Roellig, T. L., Low, F. J., et al. 2004, [ApJS](#), **154**, 1
- Winkler, H. 1992, [MNRAS](#), **257**, 677
- Woo, J.-H., Bae, H.-J., Son, D., & Karouzos, M. 2016, [ApJ](#), **817**, 108
- Woo, J.-H., Schulze, A., Park, D., et al. 2013, [ApJ](#), **772**, 49
- Wright, E. L., Eisenhardt, P. R. M., Mainzer, A. K., et al. 2010, [AJ](#), **140**, 1868
- Wu, J., Jun, H. D., Assef, R. J., et al. 2018, [ApJ](#), **852**, 96
- Wu, J., Tsai, C.-W., Sayers, J., et al. 2012, [ApJ](#), **756**, 96
- Yan, R., Newman, J. A., Faber, S. M., et al. 2006, [ApJ](#), **648**, 281
- Zakamska, N. L., & Greene, J. E. 2014, [MNRAS](#), **442**, 784
- Zakamska, N. L., Hamann, F., Pâris, I., et al. 2016, [MNRAS](#), **459**, 3144
- Zakamska, N. L., Schmidt, G. D., Smith, P. S., et al. 2005, [AJ](#), **129**, 1212
- Zakamska, N. L., Strauss, M. A., Krolik, J. H., et al. 2003, [AJ](#), **126**, 2125